

A unified computational model for cortical post-synaptic plasticity

Tuomo Mäki-Marttunen^{1*}, Nicolangelo Iannella², Andrew G Edwards¹, Gaute T Einevoll^{3,4}, Kim T Blackwell⁵

¹Simula Research Laboratory, Oslo, Norway; ²Department of Biosciences, University of Oslo, Oslo, Norway; ³Faculty of Science and Technology, Norwegian University of Life Sciences, Oslo, Norway; ⁴Department of Physics, University of Oslo, Oslo, Norway; ⁵The Krasnow Institute for Advanced Study, George Mason University, Fairfax, United States

Abstract Signalling pathways leading to post-synaptic plasticity have been examined in many types of experimental studies, but a unified picture on how multiple biochemical pathways collectively shape neocortical plasticity is missing. We built a biochemically detailed model of post-synaptic plasticity describing CaMKII, PKA, and PKC pathways and their contribution to synaptic potentiation or depression. We developed a statistical AMPA-receptor-tetramer model, which permits the estimation of the AMPA-receptor-mediated maximal synaptic conductance based on numbers of GluR1s and GluR2s predicted by the biochemical signalling model. We show that our model reproduces neuromodulator-gated spike-timing-dependent plasticity as observed in the visual cortex and can be fit to data from many cortical areas, uncovering the biochemical contributions of the pathways pinpointed by the underlying experimental studies. Our model explains the dependence of different forms of plasticity on the availability of different proteins and can be used for the study of mental disorder-associated impairments of cortical plasticity.

*For correspondence: tuomo@simula.no

Competing interests: The authors declare that no competing interests exist.

Funding: See page 32

Received: 03 February 2020

Accepted: 29 July 2020

Published: 30 July 2020

Reviewing editor: Harel Z Shouval, University of Texas Medical School at Houston, United States

© Copyright Mäki-Marttunen et al. This article is distributed under the terms of the [Creative Commons Attribution License](https://creativecommons.org/licenses/by/4.0/), which permits unrestricted use and redistribution provided that the original author and source are credited.

Introduction

Synaptic plasticity in the neocortex has been under intense research since the first observations of neocortical long-term potentiation (LTP) (Komatsu et al., 1981; Lee, 1982). Although most often studied in brain slices, synaptic plasticity in the neocortex is a key phenomenon underlying vital mammalian brain processes ranging from formation and storage of memories to attentional selection (Roelfsema and Holtmaat, 2018). These processes are impaired in heritable mental illnesses such as schizophrenia and fragile X syndrome, as well as neurodegenerative diseases such as Alzheimer's disease, all of which have been associated with deficits in cortical plasticity (Kantrowitz et al., 2017; Martin and Huntsman, 2012; Koch et al., 2014). Improved understanding of neocortical synaptic plasticity all the way from molecular to circuit level is therefore needed to further our understanding of these yet incurable diseases.

Similar to hippocampal synaptic plasticity (Larkman and Jack, 1995), synaptic plasticity in the neocortex is highly variable — the outcomes of any plasticity-inducing protocol depends on the cortical area, neuron type as well as details of the stimulation protocol (Castro-Alamancos et al., 1995; Froc and Racine, 2005; Sjöström et al., 2008; Feldman, 2009). Computational models provide a tool for efficient hypothesis testing of mechanisms of neocortical plasticity, which helps to overcome the challenges posed by excessive variability. The foundations of our mechanistic understanding of neocortical synaptic plasticity lie upon the phenomenological Bienenstock-Cooper-Munro (BCM) theory, which predicts that small synaptic activity (later attributed to small Ca²⁺ transients [Bear et al., 1987; Lisman, 1989]) cause long-term depression (LTD) whereas large synaptic activity (large Ca²⁺ transients) give rise to LTP (Bienenstock et al., 1982). Simple BCM-based models and the closely

related models of spike-timing-dependent plasticity (STDP) have been widely used to explain the emergence of input-specific cell assemblies mediating, e.g., orientation selectivity (*Shouval et al., 1997*) or memory traces (*Klampfl and Maass, 2013*) in the cortex. These models, however, typically fail to provide a mechanistic understanding of the biochemistry within the synapse — namely, they do not reveal how various molecules downstream of Ca^{2+} regulate the induction and maintenance of plasticity occurring in neuronal circuits, their composite neurons and synapses of the cortex. Moreover, current models often ignore the joint contributions of neuromodulators, which are critical for inducing some forms of cortical synaptic plasticity (*Meunier et al., 2017; Brzosko et al., 2019*). These shortcomings impede testing biochemical mechanisms of heritable mental illnesses associated with impaired cortical plasticity.

In this work, we aim at filling this gap of knowledge by introducing a biochemically detailed, mass-action law-based model of neocortical post-synaptic plasticity that can be used to study the induction of plasticity in different genetic conditions and neuromodulatory states, and under various stimulation protocols. Despite the lack of biochemically detailed models of synaptic plasticity in the neocortex, models of intracellular signalling have been used to study LTP and LTD in the hippocampus (*Bhalla and Iyengar, 1999; Jędrzejewska-Szmek et al., 2017*), cerebellum (*Gallimore et al., 2018*), and striatum (*Blackwell et al., 2019*). These models permit systematic studies on how patterns of Ca^{2+} inputs to the post-synaptic spine, either alone or in combination with neuromodulatory actions, activate different signalling pathways leading to post-synaptic plasticity in the form of, e.g., AMPA-receptor (AMPA) phosphorylation and membrane insertion. We integrate quantitative descriptions of the intracellular signalling pathways underlying synaptic plasticity in the neocortex into a unified model that is capable of describing both stimulation protocol-dependent plasticity, as well as neocortically observed neuromodulator-gated forms of STDP. We show that our model can be tuned by alterations of protein expression to reproduce not only BCM-like forms of plasticity but also experimental observations on neocortical plasticity from various cortical areas. Our results help to quantify and explain the differences in molecular constituents of different forms of neocortical LTP and LTD, and the different, data-fitted versions of our model can be directly used to examine the effects of chemical inhibitors and genetic manipulations of signalling proteins on synaptic plasticity in different cortical cells.

Results

Model construction

We reviewed the literature of molecular signalling pathways that needed for neocortical LTP/LTD, in particular in the post-synaptic spine of pyramidal cells (**Table 1A**). Three main pathways were highlighted in the experimental studies, namely, the protein kinase A (PKA), protein kinase C (PKC), and Ca^{2+} /calmodulin-dependent kinase II (CaMKII) pathways. To construct a computational model of cortical post-synaptic plasticity that describes these pathways, we adopted mass-action law-based descriptions of these pathways from biochemically detailed models of post-synaptic LTP/LTD in other brain areas, namely, hippocampus, basal ganglia and cerebellum (**Table 1B**). We prioritised the model components from hippocampal models due to the relatively small ontological differences between hippocampus and neocortex (*Kirsch and Chechik, 2016*). We focused on the effects of these pathways on AMPARs due to the better description of intracellular regulation of AMPAR dynamics in comparison to that of NMDA and kainate receptors or voltage-gated ion channels. In short, we based our model on that of *Jędrzejewska-Szmek et al., 2017*, which describes the PKA- and CaMKII-dependent phosphorylation of AMPAR subunit 1 (GluR1), and added the metabotropic glutamate receptor (mGluR) and muscarinic acetylcholine M1 receptor-mediated activation of PKC from *Kim et al., 2013* and *Blackwell et al., 2019*, respectively. Other types of receptors that interact with these pathways, such as serotonin (5HT) and dopamine receptors (*He et al., 2015*), have been shown to underlie certain types of neocortical plasticity. Dopamine D1/D5 receptors as well as serotonin 5HT4, 5HT6 and 5HT7 receptors are coupled to Gs proteins whereas 5HT2 receptors are Gq-coupled. The effects of these neurotransmitters would therefore be similar to those of norepinephrine and acetylcholine in our model (depending on the receptor composition in the post-synaptic neuron), and thus they are omitted in the present work. We then adopted the reactions describing PKC-dependent phosphorylation and endocytosis of AMPAR subunit 2 (GluR2) and

Table 1. Pathways contributing to cortical synaptic plasticity.

(A) Experimental evidence on the requirement of various molecular species for specific types of synaptic regulation in different cortical areas. (B) Model components needed for describing the modes of plasticity listed in (A). References are made to previous computational models describing these pathways. The types of phosphorylation of AMPAR subunit that mediate the plasticity are printed in bold.

(A)

Pathway components	Type of neurons	Type of regulation	Pre-/post-synaptic	References
CaMKII	Cingulate cortex	Esophageal acid-induced sensitisation	post-syn.	<i>Banerjee et al., 2013</i>
CaMKII	Prefrontal cortex, pyramidal neurons	5-HT1-induced modulation of AMPA currents	post-syn.	<i>Cai et al., 2002</i>
β -adr. receptors, PKA	Visual cortex, layer 4 pyramidal cells	Potentialiation of AMPA currents	post-syn.	<i>Seol et al., 2007</i>
M1 receptors, PKC	Visual cortex, layer 4 pyramidal cells	Depression of AMPA currents	post-syn.	<i>Seol et al., 2007</i>
D1-PKA	Prefrontal cortex, pyramidal neurons	Potentialiation of AMPA currents	post-syn.	<i>Sun et al., 2005</i>
β -adr. receptors	Frontal cortex	Potentialiation of field EPSPs	n/a	<i>Sáez-Briones et al., 2015</i>
PKC	Cultured cortical neurons	Internalisation of AMPARs	post-syn.	<i>Chung et al., 2000</i>
ERK	Visual cortex	Potentialiation of field EPSPs	n/a	<i>Di Cristo et al., 2001</i>

(B)

Molecular pathway	Cell type and references
$\text{Ca}^{2+} \rightarrow \text{CaM} \rightarrow \text{CaMKII}$	Hippocampal CA1 neuron <i>Bhalla and Iyengar, 1999; Jędrzejewska-Szmek et al., 2017</i> , generic <i>Hayer and Bhalla, 2005</i> , cerebellar Purkinje cells <i>Gallimore et al., 2018</i> , striatal spiny projection neuron <i>Blackwell et al., 2019</i>
$\text{CaMKII} \rightarrow \text{GluR1 S831p}$	Hippocampal CA1 neuron <i>Jędrzejewska-Szmek et al., 2017</i>
β -adrenergic receptors \rightarrow cAMP	Hippocampal CA1 neuron <i>Jędrzejewska-Szmek et al., 2017</i>
cAMP \rightarrow PKA	Hippocampal CA1 neuron <i>Bhalla and Iyengar, 1999; Jędrzejewska-Szmek et al., 2017</i> , cerebellar Purkinje cells <i>Gallimore et al., 2018</i>
$\text{PKA} \rightarrow \text{GluR1 S845p}$	Hippocampal CA1 neuron <i>Jędrzejewska-Szmek et al., 2017</i>
M1 receptors \rightarrow PLC	Cerebellar Purkinje cells <i>Gallimore et al., 2018</i>
PLC \rightarrow PKC	Hippocampal CA1 neuron <i>Bhalla and Iyengar, 1999</i> , striatal spiny projection neuron <i>Kim et al., 2013; Blackwell et al., 2019</i> , cerebellar Purkinje cells <i>Kotaleski et al., 2002; Gallimore et al., 2018</i>
$\text{PKC} \rightarrow \text{GluR2 S880p}$	Cerebellar Purkinje cells <i>Gallimore et al., 2018</i>

reinsertion to the membrane from *Gallimore et al., 2018*, which allowed the representation of post-synaptic depression with our model. The pathways included in the model are illustrated in *Figure 1*. A description of the model calibration is given in Materials and methods, section 'Construction and calibration of the biochemically detailed model of post-synaptic plasticity in the cortex', and the full set of model reactions and initial concentrations is provided in Tables 3 and 4, respectively.

Ca²⁺ activates multiple pathways that regulate the post-synaptic plasticity in cortical PCs

All pathways of *Table 1B* are Ca²⁺-dependent, but due to the variability in binding rates and quantities of different Ca²⁺-binding molecules, some pathways become more easily activated than others. This permits LTP or LTD to be induced in a way that is sensitive to the amount of Ca²⁺ inputs and may serve as a basis for BCM-type rules of plasticity.

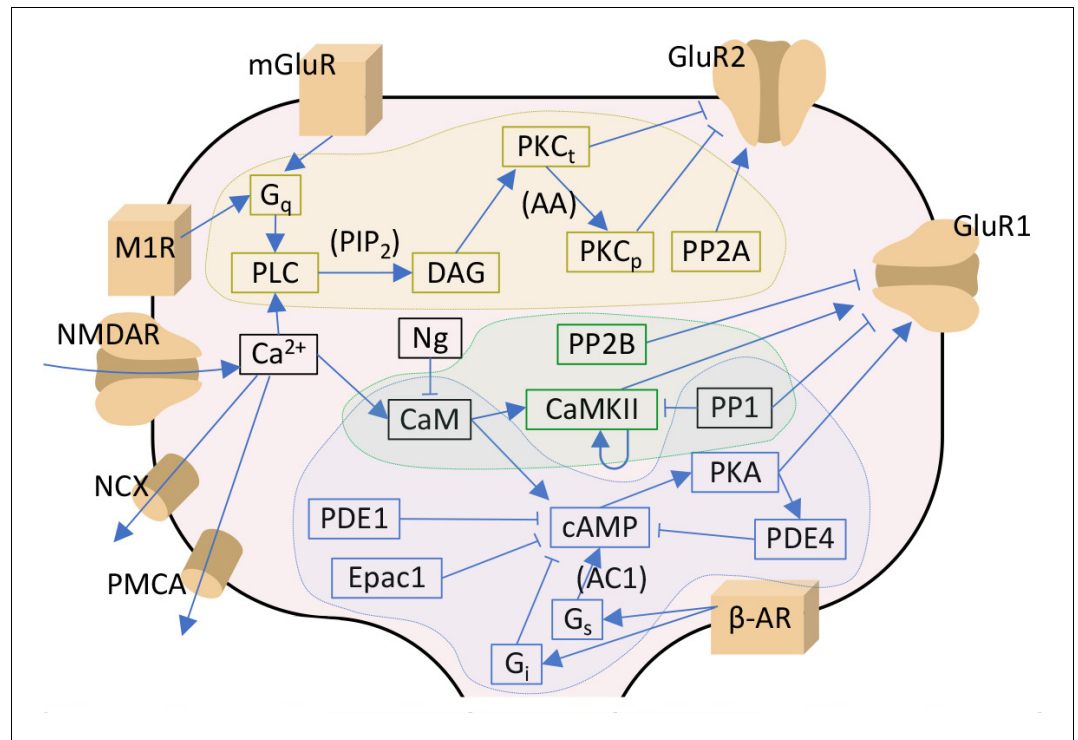


Figure 1. Signalling pathways included in the model. The PKA-pathway-related proteins and signalling molecules are highlighted by blue, PKC-pathway molecules by yellow, and CaMKII-pathway molecules by green colours. Reactions associated with a molecular species in parenthesis indicate a dependency on the denoted species — for details, see **Table 3**. Acronyms: β -AR – β -adrenergic receptor; AC1 and AC8 – adenylyl cyclase type 1 or 8; CaM – calmodulin; CaMKII – calmodulin-dependent protein kinase II; cAMP – cyclic adenosine monophosphate; DAG – diacylglycerol; Epac1 – exchange factor directly activated by cAMP 1; Gi, Gq and Gs – G-protein type I, Q, or S; GluR1 and GluR2 – AMPAR subunit 1 or 2; mGluR – metabotropic glutamate receptor; M1R – cholinergic receptor M1; NCX – Na^+ - Ca^{2+} exchanger; Ng – neurogranin; NMDAR – NMDA receptor; PDE1 and PDE4 – phosphodiesterase type 1 or 4; PIP₂ – phosphatidylinositol 4;5-bisphosphate; PKA – protein kinase A; PKCt and PKCp – transiently or persistently active protein kinase C; PLC – phospholipase C; PMCA – plasma membrane Ca^{2+} ATPase; PP1 – protein phosphatase 1; PP2A – protein phosphatase 2A; PP2B – protein phosphatase 2B (calcineurin). In this work, the NMDARs are considered only in section ‘Paired pre- and post-synaptic stimulation induces PKA- and PKC-dependent spike-timing-dependent plasticity (STDP) in GluR1-GluR2-balanced synapses’: in the rest of the work, Ca^{2+} is directly injected as a square-pulse current into the spine.

To examine the sensitivities of LTP- and LTD-inducing pathways to Ca^{2+} , we simulated the injection of a prolonged square-pulse Ca^{2+} input of varying magnitude (illustrated in **Figure 2A**) into the post-synaptic spine and quantified the degree of activation of each of the Ca^{2+} -binding molecules and the downstream signalling cascades. The simulations were carried out in the presence of mGluRs and β -adrenergic and cholinergic neuromodulation, which were modelled as prolonged square-pulse inputs as well.

The injected Ca^{2+} quickly bound to Ca^{2+} buffers (immobile buffer and calbindin, **Figure 2B**) and pumps (PMCA and NCX, **Figure 2C**) as well as to the proteins of the PKC pathway (phospholipase A2 (PLA2) and C (PLC), **Figure 2D**): a 95% saturation was reached in 1–2 s (**Figure 2B–D**). In contrast, the activation of calmodulin (CaM) was slower (**Figure 2E**): a 95% saturation was reached in 32–53 s, depending on the magnitude of the Ca^{2+} input. Consistent with experimental literature, a vast majority of Ca^{2+} was quickly bound and only a small fraction remained free in the cytosol (**Figure 2F**).

To further illustrate the differences between the activation patterns of these pathways, we quantified the degrees of Ca^{2+} binding of these molecules in a steady state (5 min after the onset of Ca^{2+}) and the overall activation/deactivation of downstream molecules as a function of the magnitude of the Ca^{2+} injection. Both PKC pathway-mediating proteins PLC, diacylglycerol lipase (DGL), and

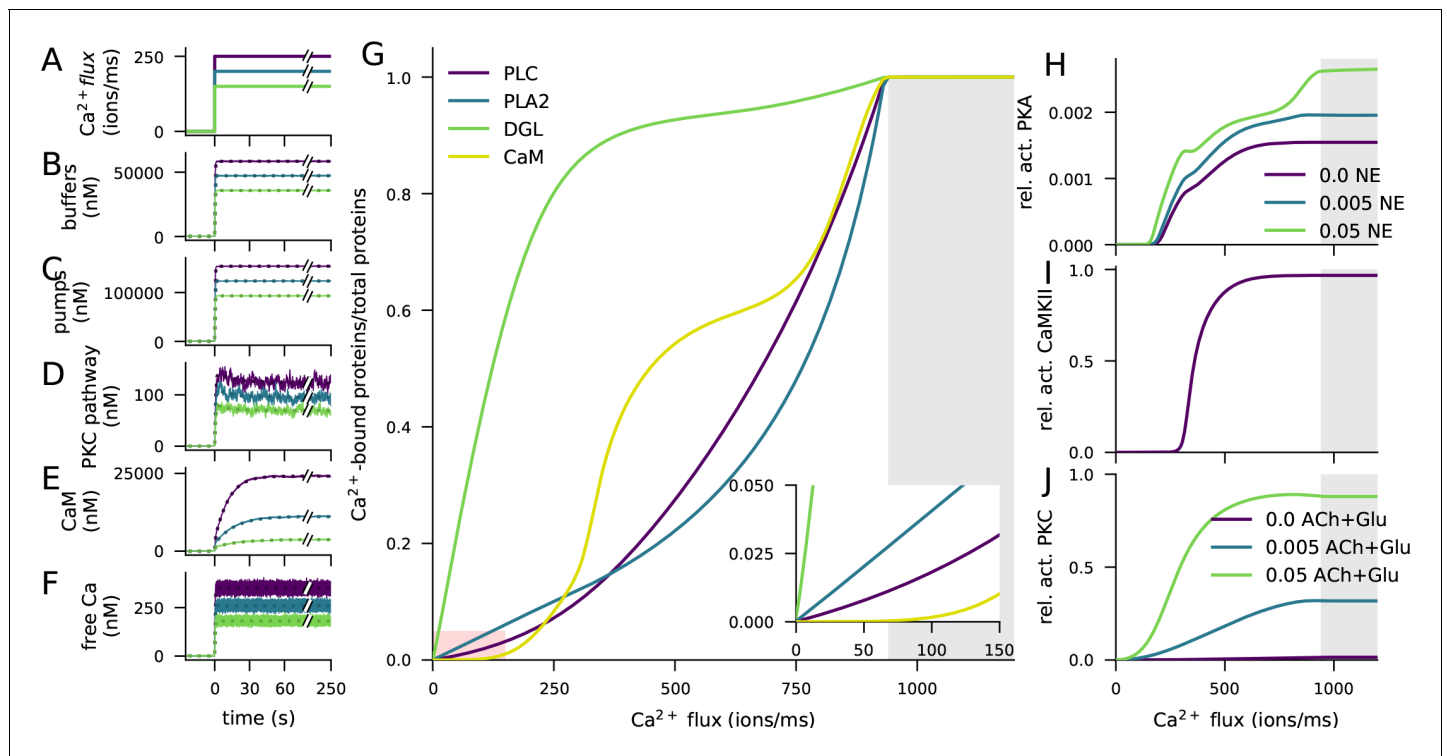


Figure 2. Ca^{2+} activates CaMKII, PKA, and PKC pathways. (A) Illustration of the stimulus protocols with Ca^{2+} flux amplitudes 150 (green), 200 (cyan), and 250 (purple) particles/ms. (B–F) Time courses of Ca^{2+} (in nM) bound to buffers (B), pumps (C), PKC-pathway proteins (D), or CaM (E), and the concentration of free Ca^{2+} ions (F), according to NeuroRD (solid; averaged across eight samples) or NEURON (dashed) simulations. Colours indicate the Ca^{2+} flux used (see A). (B) Number of Ca^{2+} ions bound to Ca^{2+} buffers, that is immobile buffer and calbindin. (C) Number of Ca^{2+} ions bound to Ca^{2+} pumps and exchangers, that is PMCA and NCX. (D) Number of Ca^{2+} ions bound to PKC-pathway proteins PLC and PLA2. (E) Number of Ca^{2+} ions bound to CaM, in all its forms. (F) Cytosolic Ca^{2+} concentration (mM) (G) Degrees of activation of different Ca^{2+} -binding proteins in a steady state (5 min after onset of Ca^{2+} input) as a function of the magnitude of Ca^{2+} flux. The x-axis shows the amplitude of the Ca^{2+} input (see panel A), and the y-axis shows the ratio of the underlying species in a Ca^{2+} -bound form over the total number of the proteins. For CaM, only the CaM molecules bound by four Ca^{2+} ions are considered activated — in PLC, PLA2, and DGL, binding of only one Ca^{2+} ion is needed for activation. Here, the measured quantity of active PLC includes both Gq-bound and non-Gq-bound CaPLC. Inset: zoomed-in view on the red area. (H) Ratio of the steady-state concentration of PKA catalytic subunit over the theoretical maximum where all PKA molecules were dissociated into residuals and catalytic subunits. Colour of the curve indicates the amplitude of the β -adrenergic ligand flux (particles/ms). (I) Fraction of phosphorylated CaMKII subunits. (J) Fraction of (transiently or persistently) activated PKC. Colour of the curve indicates the amplitude of the cholinergic and glutamatergic ligand flux (particles/ms). The grey area in panels (G–J) represents Ca^{2+} inputs that cause cytosolic Ca^{2+} concentration to reach extremely high levels (>1 mM) that are likely to lead to apoptosis.

PLA2, along with the PKA and CaMKII pathway-related protein CaM became completely activated if large enough Ca^{2+} flux is given, but their degrees of activity varied across the magnitude of the injected Ca^{2+} flux (Figure 2G). DGL was most completely activated throughout the Ca^{2+} amplitude, owing to the large equilibrium constant of its Ca^{2+} binding. At extremely large Ca^{2+} fluxes, CaM was more completely bound by Ca^{2+} than PLC and PLA2 (Figure 2G), but at lower Ca^{2+} amplitudes, CaM remained largely unbound (Figure 2G inset). This is reflected in the activation patterns of the catalytic subunit of PKA (Figure 2H) and CaMKII (Figure 2I), both of which are dependent on the activation of CaM and thus had a small response at low Ca^{2+} amplitudes. PKC, by contrast, became activated at relatively small Ca^{2+} amplitudes (Figure 2J). Of these three pathways, the PKC pathway was dependent on the cholinergic ligands or the activation of the mGluRs (Figure 2J), and the PKA pathway was dependent on the availability of β -adrenergic ligands (Figure 2H). Taken together, these results highlight the need for large Ca^{2+} flux to the post-synaptic spine for the activation of the CaMKII pathway, relatively large Ca^{2+} flux for the activation of the PKA pathway, and relatively small Ca^{2+} flux for the activation of the PKC pathway.

High-frequency stimulation (HFS) causes LTP and low-frequency stimulation (LFS) causes LTD in GluR1-GluR2-balanced synapses

The Ca^{2+} flux entering the post-synaptic spine is extremely large during and after synaptic transmission and low otherwise, which causes the signalling pathways to be activated and deactivated in a more dynamic way than described in the previous section (' Ca^{2+} activates multiple pathways that regulate the post-synaptic plasticity in cortical PCs'). The activation of these pathways and their dependence on the stimulus protocol are difficult to study experimentally due to methodological constraints (e.g., side effects of fluorescence indicators, lack of signal calibration, and poor temporal or spatial resolution), but biochemically detailed models, such as the one considered in this work, can provide insights into the transient molecular mechanisms behind LTP and LTD. Our model is particularly well suited to study the mechanisms behind CaMKII-, PKA- and PKC-mediated phosphorylation of AMPAR subunits, which are important mediators of long-term plasticity (Wang et al., 2005). Phosphorylation of GluR1 subunits at S845 increases the insertion rate of the AMPAR into the membrane, thus leading to post-synaptic LTP (Diering et al., 2016). Conversely, phosphorylation of GluR2 subunits at S880 increases the rate of receptor endocytosis from the membrane, and has thus been observed to lead to post-synaptic LTD (Xia et al., 2000). However, it is not the number of the membrane-expressed AMPAR subunits alone that determine the strength of the synapse, but different compositions of the subunits have different single-channel conductances, and phosphorylation at S831 of the GluR1 subunit also affects the conductance of the channel (Oh and Derkach, 2005).

To simulate the reaction dynamics in the post-synaptic spine under realistic input patterns, we applied the 4xHFS and LFS protocols. Each input contained transient (3 ms) influxes of Ca^{2+} (1900 particles/ms) into the cytosol and glutamate (20 particles/ms), acetylcholine (20 particles/ms) and β -adrenergic ligand (10 particles/ms) into the extracellular subspace near the spine membrane. We used a balanced ratio (1:1) of GluR1 and GluR2 subunits. We recorded the time courses of the concentrations of all CaMKII-, PKA-, and PKC-pathway molecules contributing to LTP or LTD to monitor their activity during and following the stimulation protocols. We also recorded the numbers of membrane-inserted GluR1 and GluR2 and their state of phosphorylation and used Equation 5 for determining the maximal synaptic conductance.

In the 4xHFS protocol, which typically causes LTP in plasticity experiments, our model predicts a large increase in total synaptic conductance (Figure 3A) due to a radical increase in membrane-inserted GluR1 subunits (Figure 3B) and a decrease in GluR2 subunits (Figure 3C). These changes in membrane-expression of AMPAR subunits were dependent on activations of many signalling proteins in the CaMKII (Figure 3D–H), PKA (Figure 3I–M), and PKC (Figure 3N–R) pathways. First, the Ca^{2+} entry (Figure 3D) caused a rapid increase in half-activated calmodulin (bound by two Ca^{2+} ions; Figure 3E), leading to a longer-lasting increase in active calmodulin (Figure 3F). Calmodulin activation led to an increase in the concentration of phosphorylated CaMKII (Figure 3G), which phosphorylated the GluR1-type receptors at S831 (Figure 3H). The β -adrenergic input (Figure 3I), in turn, bound to the β -adrenergic receptors and activated the Gs proteins (Figure 3J), which bound to the adenylyl cyclase AC1 to produce cyclic adenosine monophosphate (cAMP, Figure 3K). cAMP bound to PKA to release the catalytic subunits of PKA (Figure 3L), which led to a phosphorylation of the GluR1-type receptors at S845 (Figure 3M) and thus to increased membrane expression of GluR1 subunits and total synaptic conductance (Figure 3A–B). Due to the simultaneous activation of the CaMKII pathway, a significant proportion of double phosphorylated GluR1-type receptors was observed (Figure 3H,M). As for the PLC–PKC pathway, glutamate (Figure 3N, blue) bound to mGluRs and acetylcholine (Figure 3N, green) bound to muscarinic receptors (M1), and the activation of these receptors contributed to the activation of Gq proteins (Figure 3O). The activated Gq proteins bound with PLC and metabolised phosphatidylinositol 4,5-bisphosphate (Pip2) into diacylglycerol (DAG, Figure 3P), which activated PKC (Figure 3Q). This led to the phosphorylation of GluR2-type receptors at S880 (Figure 3R), which caused the decrease in membrane expression of GluR2 observed in Figure 3C.

The differences between NEURON and NeuroRD simulation results in Figure 3M were due to the stochasticity in NeuroRD simulator — both smaller and larger GluR1 phosphorylation levels compared to NEURON simulation results (Figure 3M, dashed) were obtained when NeuroRD simulations were run with different random number seeds (not shown).

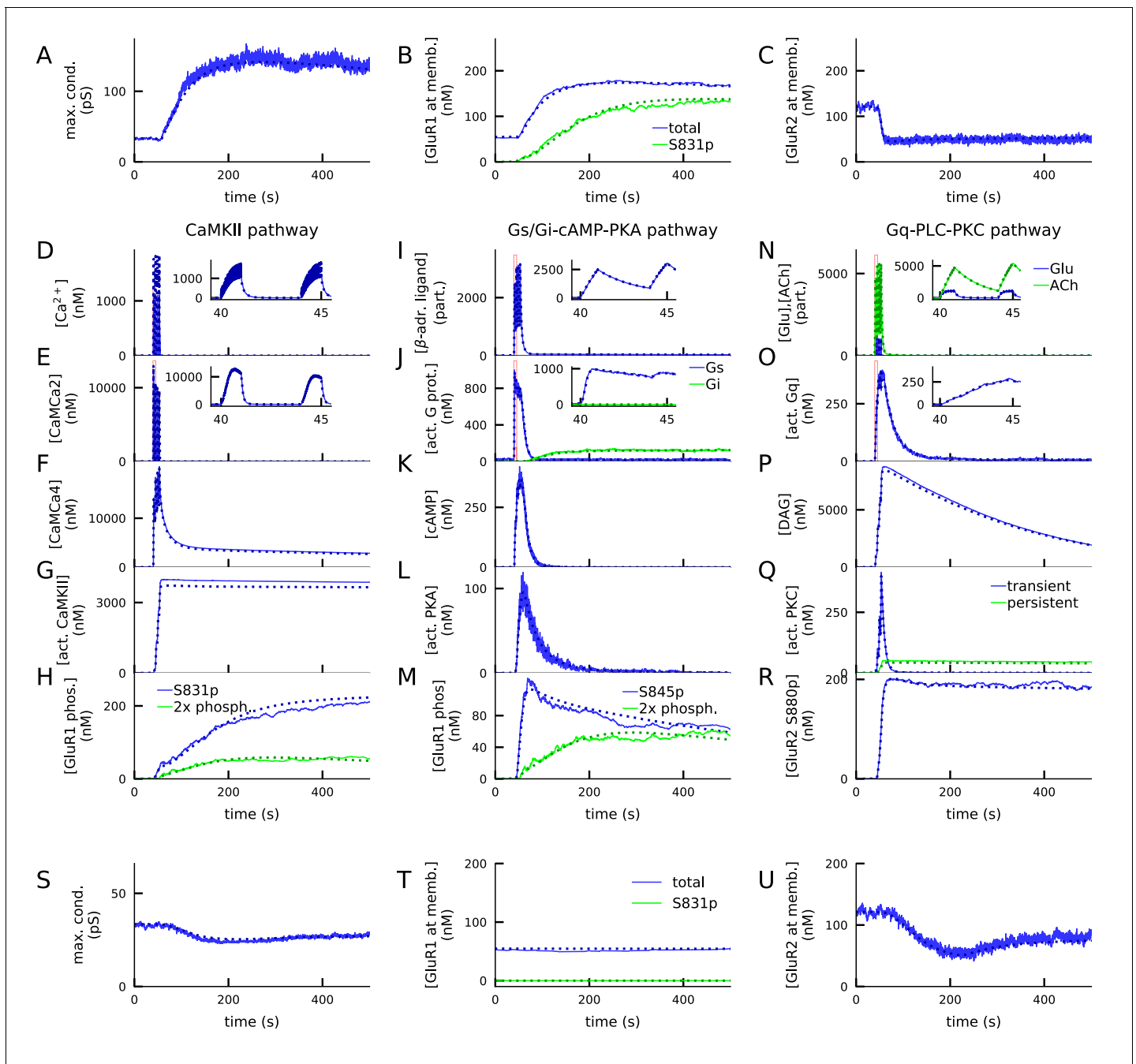


Figure 3. 4xHFS activates CaMKII, PKA, and PKC pathways and leads to LTP (A–R), while LFS activates the PKC pathway and leads to LTD (S–U). (A) Total synaptic conductance in response to 4xHFS, determined by the numbers of membrane-inserted GluR1s and GluR2s — see **Equation 5**. The stimulation starts at 40 s and lasts until 53 s. (B–C) Concentration of membrane-inserted GluR1s (B) and GluR2s (C) in response to 4xHFS. (D–H) Concentration of different species in the CaMKII pathway, namely, intracellular unbound Ca^{2+} (D), CaM bound with two Ca^{2+} ions (E), CaM bound with four Ca^{2+} ions (active CaM; F), phosphorylated CaMKII, bound or unbound by CaMCA4 (G), and S831-phosphorylated and double-phosphorylated GluR1 subunits (H) in response to 4xHFS. (I–M) Concentration of different species in the cAMP-PKA pathway, namely, β -adrenergic ligand in all its forms (I), activated (GTP-bound but not bound to ATP) Gs and Gi proteins (J), intracellular cAMP (K), catalytic subunit of PKA (L), and S845-phosphorylated and double-phosphorylated GluR1 subunits (M) in response to 4xHFS. (N–R) Concentration of different species in the PLC-PKC pathway, namely, glutamate and acetylcholine in all their forms (N), activated (GTP-bound but not bound to DAG) Gq proteins (O), intracellular DAG (P), activated PKC (Q), and S880-phosphorylated GluR2 subunits (R) in response to 4xHFS. S: Total synaptic conductance in response to LFS. (T–U) Concentration of membrane-inserted GluR1s (T) and GluR2s (U) in response to LFS, which starts at 40 s and lasts until 220 s. The solid lines represent stochastic (NeuroRD) simulation results, while the dashed lines represent data from deterministic (NEURON RxD) simulations. β -adrenergic ligands, glutamate, *Figure 3 continued on next page*

Figure 3 continued

and acetylcholine are measured in numbers of particles as they reside both at the membrane (when bound to receptors) and at the extracellular subspace near the spine membrane (when unbound); other species measured in concentration.

The online version of this article includes the following figure supplement(s) for figure 3:

Figure supplement 1. Both GluR1 and GluR2 are needed for bidirectional plasticity.

Figure supplement 2. An alternative dimers-of-like-dimers rule of tetramer formation reproduces the HFS-induced LTP, LFS-induced LTD, and STDP predictions obtained with the default tetramer formation rule.

Figure supplement 3. The biochemical signalling network model, given the NMDAR-conducted Ca^{2+} inputs from the multicompartmental neuron model of layer 2/3 pyramidal cell under 1.3 mM extracellular $[\text{Mg}^{2+}]$, predicts LTP for 6xHFSt and LTD for LFS-1Hz.

Figure supplement 4. The biochemical signalling network model robustly predicts LTP for HFS and LTD for LTP with altered durations of neuromodulatory inputs.

In the LFS protocol, which typically causes LTD in the experiments, our model predicts a prominent (20%) decrease in total synaptic conductance (**Figure 3S**) due to a decrease in GluR2 subunits. In this protocol, the Ca^{2+} inputs are insufficiently large to activate CaM, and the Gs proteins remain deactivated as well (data not shown). In consequence, CaMKII and PKA pathways remain deactivated, and the effect of the LFS protocol on GluR1 phosphorylation and membrane insertion is small (**Figure 3T**). By contrast, the PKC pathway is almost as strongly activated as in the 4xHFS protocol (data not shown), leading to prominent S880 phosphorylation of GluR2 (data not shown) and removal of GluR2 from the membrane (**Figure 3U**).

The expression of both LFS-induced LTD and 4xHFS-induced LTP of these types is dependent on the presence of both GluR1 and GluR2 subunits: GluR1-deficient synapses failed to show 4xHFS-induced LTP (**Figure 3—figure supplement 1A**) and GluR2-deficient synapses failed to show LFS-induced LTD (**Figure 3—figure supplement 1B**). To show that our results were not an artefact of the tetramer formation rule (**Equation 1–5**), we applied an alternative tetramer formation rule where GluR1 and GluR2 subunits randomly dimerised and the dimers paired with like dimers (which disallows the emergence of heterotetramers with 1:3 or 3:1 proportion of GluR1:GluR2 subunits; **Gan et al., 2015**). We reproduced the LFS-induced LTD and 4xHFS-induced LTP using this dimer-of-like-dimers rule with a modified (35:65) balance of GluR1 vs. GluR2 subunits (**Figure 3—figure supplement 2A**).

In the above analyses, we used brief square-pulse fluxes of Ca^{2+} to the synapse model, which is a simple representation of inputs during synaptic plasticity induction protocols. Alternatively, Ca^{2+} current entering the post-synaptic spines can be estimated by using multicompartmental biophysically detailed neuron models. We simulated a model of layer 2/3 pyramidal cell, stimulated with synaptic inputs from a 6xHFSt or LFS-1Hz protocol (see Materials and methods, section 'Modelling the Ca^{2+} inputs and neuromodulatory inputs'), to determine the Ca^{2+} inputs entering the post-synaptic spine through NMDA receptors (NMDARs). In accordance with **Figure 3** and experimental data from somatosensory cortex (**Heusler et al., 2000**), our model predicted that 6xHFSt induced LTP whereas LFS-1Hz induced LTD (**Figure 3—figure supplement 3**). Here, the 6xHFSt protocol was used instead of 4xHFS to model the same protocol as in **Heusler et al., 2000**; our model would also predict an LTP for 4xHFS (data not shown). The HFS-induced LTP and LFS-induced LTD of **Figure 3** could also be reproduced with alternative durations of neuromodulator inputs, including 10 min bath applications (**Figure 3—figure supplement 4**). These results indicate that our model can reproduce HFS-induced LTP and LFS-induced LTD also when using realistic NMDAR-conducted Ca^{2+} transients and that these forms of plasticity are robust to the temporal profile of the neuromodulatory inputs.

The activations of the above pathways are dependent on the magnitude and dynamics of the inputs to the model, namely, Ca^{2+} , β -adrenergic and cholinergic ligands, and glutamate. All pathways leading to GluR1 and GluR2 phosphorylation and the consequent exocytosis and endocytosis are Ca^{2+} -dependent: blocking Ca^{2+} entry completely abolished 4xHFS-induced LTP (**Figure 4A**) that followed GluR1 insertion (**Figure 4B**) and GluR2 endocytosis (**Figure 4C**). Blocking β -adrenergic ligands abolished the 4xHFS-induced LTP (**Figure 4A**) by suppressing the membrane-insertion of GluR1 (**Figure 4B**), but had no effect on GluR2 endocytosis (**Figure 4C**). Likewise, blocking β -adrenergic ligands had no effect on LFS-induced LTD (not shown). In contrast, LFS-induced LTD (**Figure 4E**) that followed GluR2 endocytosis (**Figure 4G**) was reduced by blockade of mGluR activation while the number of GluR1 subunits at the membrane remained unaffected (**Figure 4F**). This

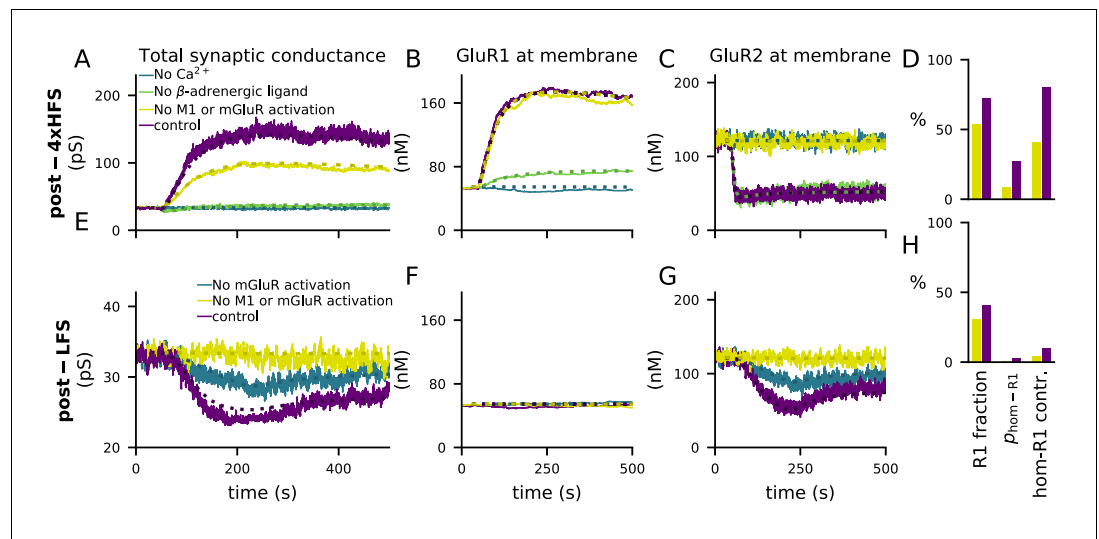


Figure 4. 4xHFS-induced LTP is dependent on β -adrenergic ligands and LFS-induced LTD is dependent on activation of mGluRs or cholinergic receptors. (A–D) 4xHFS-induced LTP in the control case (dark purple), without Ca^{2+} inputs (blue), without β -adrenergic ligands (green), and under blockade of PKC pathway-activation (mGluRs or cholinergic receptors; yellow). (E–H) LFS-induced LTD in the control case (dark purple), under the blockade of mGluR activation (blue), and under blockade of both mGluRs or cholinergic receptors (yellow). (A, E) Total synaptic conductance. (B, F) Membrane expression of GluR1. (C, G) Membrane expression of GluR2. (D, H) The fraction of membrane-inserted GluR1 over all membrane-inserted GluR subunits (left), the probability of an AMPAR tetramer being homomeric GluR1 (middle), and the relative contribution of homomeric GluR1 subunits to the total conductance (i.e., summed conductance of homomeric GluR1 tetramers divided by the summed conductance of all tetramers; right). The bars represent the values at the end of the 4xHFS (D) or LFS (H) simulation with (dark purple) and without (yellow) PLC-activating ligands.

reduction was strengthened by simultaneous blockade of cholinergic inputs (Figure 4E–G, yellow traces). Counterintuitively, blocking mGluR and M1-receptor activation also reduced the amplitude of the 4xHFS-induced LTP (Figure 4A) by disabling GluR2 endocytosis (Figure 4C) while it had no effect on GluR1 insertion (Figure 4B). The reason for this is that in the PKC pathway-blocked case there is a smaller post-4xHFS membrane-bound GluR1 ratio (fraction of GluR1 subunits over all GluR subunits at the membrane) than in the control case, and thus the probability of AMPARs being homomeric GluR1 tetramers (which had a very large conductance compared to other tetramers; Equation 5) is much smaller in the former case than in control (Figure 4D). Although qualitatively similar difference can be observed in post-LFS membrane-bound GluR1 ratios between PKC pathway-blocked case and control, the probability of homomeric GluR1 tetramers and their contribution to the synaptic conductance are very small in both cases (Figure 4H) and thus the LFS-induced LTD is not affected.

Taken together, our results show that cortical synapses expressing both GluR1 and GluR2 subunits can express a frequency-dependent form of post-synaptic plasticity (LTP for high-frequency inputs, LTD for low-frequency inputs) that is gated by neuromodulators affecting the PKA and PKC pathways. Our findings also lend support to that GluR2 endocytosis may lead to either potentiation (Figure 4A) or depression (Figure 4E), depending on the prevalence of the GluR1 subunits at the membrane.

Paired pre- and post-synaptic stimulation induces PKA- and PKC-dependent spike-timing-dependent plasticity (STDP) in GluR1-GluR2-balanced synapses

Cortical synapses typically exhibit a type of synaptic plasticity, namely STDP, that is dependent on both the pre- and post-synaptic activity. According to a classical model, the differences in the outcome of STDP for different pairing intervals of pre- and post-synaptic stimulus are explained by different amount of Ca^{2+} entering the post-synaptic spine, which is affected by both the pre-

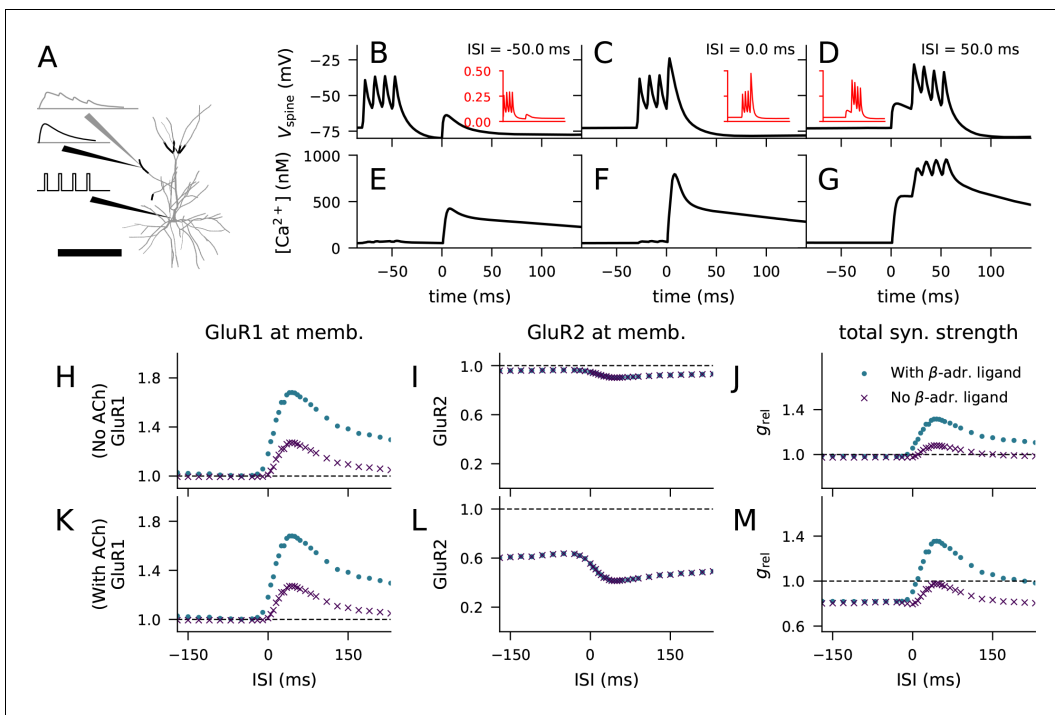


Figure 5. Layer 2/3 pyramidal cell plasticity in response to STDP protocol depends on neuromodulatory state and pairing interval. (A) Layer 2/3 pyramidal cell morphology (grey, thin), locations of synaptic input highlighted (black, thick). Inset: Illustration of the inputs (black) and the recorded synaptic intracellular Ca^{2+} (grey). Scale bar 200 μm . (B–D) Membrane potential at the dendritic spine when the pre-synaptic stimulation onset is 50 ms after (B), at the same time as (C), or 50 ms prior to (D) the onset of the last somatic stimulus. Inset (red): Mg^{2+} -gate variable as a function of time, ranging from -80 ms to 140 ms in a similar manner as the data in the main panel. (E–G) Concentration of free Ca^{2+} in the dendritic spine according to the biochemical spine model when the pre-synaptic stimulation onset is 50 ms after (B), at the same time as (C), or 50 ms prior to (D) the onset of the last somatic stimulus. (H–J) No LTD was induced by the stimulation protocol (1 Hz paired with post-synaptic stimulation for 2 min) in the absence of M1-receptor activation, but pairing-interval-dependent LTP was induced in presence of β -adrenergic inputs. (K–M) Pairing-interval-dependent LTD was induced when the synaptic input was coupled with cholinergic inputs, and STDP was induced when both cholinergic and β -adrenergic inputs were present. (H, K) Relative concentration of GluR1 at the membrane 16 min after the stimulation onset (normalised by concentration of membrane-inserted GluR1 at rest). (I, L) Relative concentration of GluR2 at the membrane 16 min after the stimulation onset (normalised by concentration of membrane-inserted GluR2 at rest). (J, M) Relative synaptic conductance (Equation 5) 16 min after the stimulation onset (normalised by synaptic conductance at rest).

The online version of this article includes the following figure supplement(s) for figure 5:

Figure supplement 1. Ca^{2+} fluxes predicted by the multicompartmental layer 2/3 pyramidal cell model depend on the inter-stimulus interval (ISI).

synaptically released glutamate and the elevation of post-synaptic membrane potential. Biophysically detailed neuron modelling offers a powerful tool for determining the size of these Ca^{2+} inputs as a function of the pairing interval.

We considered the LTP/LTD response to paired stimulation protocol using a multicompartmental model of a layer 2/3 pyramidal cell (Figure 5A; Markram et al., 2015). We placed a synaptic spine with volume $0.5 \mu\text{m}^3$ at a random location on the apical dendrite, 250–300 μm from the soma (Figure 5A, thick, black branches), and stimulated the head of the spine with glutamatergic synaptic currents (Hay and Segev, 2015; Markram et al., 2015; Figure 5A, black traces, top). In parallel, we stimulated the soma with a burst of four short (2 ms) supra-threshold square-pulse currents (Figure 5A, black traces, bottom). Given that approximately 10% of the NMDAR-mediated currents and none of the AMPAR-mediated currents are conducted by Ca^{2+} flux, we could determine the number of Ca^{2+} ions entering the spine at each time instant following the onset of the synaptic input (Figure 5A, grey traces). This experiment was repeated using different inter-stimulus intervals (ISI) between the synaptic and somatic stimuli and averaged across $N_{\text{samp}} = 200$ trials. The membrane potential dynamics at the post-synaptic spine depended on the ISI (Figure 5B–D), largest effects response being obtained with near-coincident stimuli (Figure 5C). The higher the membrane

potential at the spine, the higher the value of the variable describing the Mg^{2+} -gate opening in the NMDA receptor (**Figure 5B–D**, insets) (Hay and Segev, 2015; Markram et al., 2015). Thus, the Ca^{2+} flux time course varied across the pairing ISIs (**Figure 5—figure supplement 1**). These Ca^{2+} flux time series were imported into our biochemical model (Ca^{2+} transients in the spine model showed in **Figure 5E–G**), which allowed us to predict the magnitude of GluR subunit phosphorylation and membrane insertion for each pairing interval. When added as bath application, the β -adrenergic and cholinergic ligands were simulated by prolonged injections of 50 particles/s for 10 min, starting 8 min before the STDP protocol — these neuromodulators alone (without the electric stimulation-mediated Ca^{2+} inputs) did not cause synaptic plasticity. Throughout the experiments, the activation of mGluRs was blocked.

We first confirmed that the membrane expression of the glutamate receptors was not strongly affected by paired synaptic and somatic stimulation in the absence of β -adrenergic (which activates the PKA pathway) and cholinergic (which activates the PKC pathway) neuromodulation. Our model predicted that there is little change in the membrane expression of GluR1 and GluR2 type receptor subunits in this stimulation protocol (**Figure 5H–I**, purple). Consequently, our model reproduced the observation (Seol et al., 2007) that this stimulation protocol led to little change in predicted synaptic conductance (**Figure 5J**, purple).

We next considered the paired synaptic-somatic stimulation in the presence of β -adrenergic ligand. Our model predicted a prominent (up to 70%) increase in GluR1 membrane expression with little effect on GluR2 membrane expression (**Figure 5H–I**, blue). The predicted increase in GluR1 membrane expression (**Figure 5H**) and the consequent increase in synaptic conductance (**Figure 5J**, blue) were most prominent when the ISI was around 20–80 ms, and modest for large ISIs. These predictions are consistent with the experiments where an ISI-dependent potentiation of the EPSCs in the presence of β -adrenergic receptor agonists and absence of cholinergic agonists was observed (Seol et al., 2007).

When β -adrenergic neurotransmission was blocked but M1 receptors were activated by cholinergic ligands, the model predicted a prominent (up to 60%) decrease in GluR2 membrane expression, with little effect on GluR1 membrane expression (**Figure 5K–L**, purple). Our model of synaptic conductance (**Equation 5**) predicted a decrease in total conductance in a GluR1-GluR2-balanced synapse for this condition (**Figure 5M**, purple), which is in line with the experimental data (Seol et al., 2007). The depression takes place throughout the tested ISIs, but the effect was smallest for ISIs very close to zero due to the counteracting effects of GluR1 membrane-insertion (**Figure 5K**, purple). Finally, when both β -adrenergic and cholinergic neurotransmission were active, our model predicted an increased GluR1 membrane expression and decreased GluR2 membrane expression, both of which were ISI dependent (**Figure 5K–L**, blue). In these simulations, the predicted synaptic conductance was increased for small and moderate pre-post intervals and decreased otherwise (**Figure 5M**, blue), which is qualitatively similar to experimental data (Seol et al., 2007). These results are dependent on the availability of both GluR1 and GluR2 subunits at the post-synaptic spine: in simulations where GluR1 or GluR2 subunits were absent, only LTD (**Figure 3—figure supplement 1C**) or LTP (**Figure 3—figure supplement 1D**), respectively, was induced by the STDP protocol. In a similar manner as the HFS- and LFS-induced plasticity in **Figure 3—figure supplement 2A**, we could reproduce the STDP using the dimer-of-like-dimers tetramer formation rule with a GluR1 fraction of 35% (**Figure 3—figure supplement 2B**). Taken together, our model with balanced numbers of GluR1 and GluR2 subunits reproduces the neuromodulator-gated STDP observed in layer 2/3 pyramidal cells of the visual cortex.

The combination of our biochemically detailed model with the biophysically detailed model of layer 2/3 pyramidal cell model provides a compelling means of hypothesis testing for cortical STDP in this cell type. We analyzed how the shape of the STDP curve of **Figure 5M** is affected by the number of spikes in each post-synaptic burst stimulus. Our simulations suggest that decreasing the number of spikes per burst decreases the amplitude of both LTP and LTD in the STDP protocol and, in particular, brings the LTD for large post-pre ISIs close to zero (**Figure 6A**). These alterations are mediated by changes in both the level of membrane-insertion of GluR1 and endocytosis of GluR2 subunits (**Figure 6A**, insets). For small and moderate pre-post ISIs, the effects of decreasing the number of post-synaptic stimuli on the STDP curve are expected: both GluR1 insertion and GluR2 endocytosis are of smaller amplitude, and hence the dampened LTP amplitude (**Figure 6A**). By contrast, for post-pre ISIs and large pre-post ISIs, decreasing the number of post-synaptic stimuli results

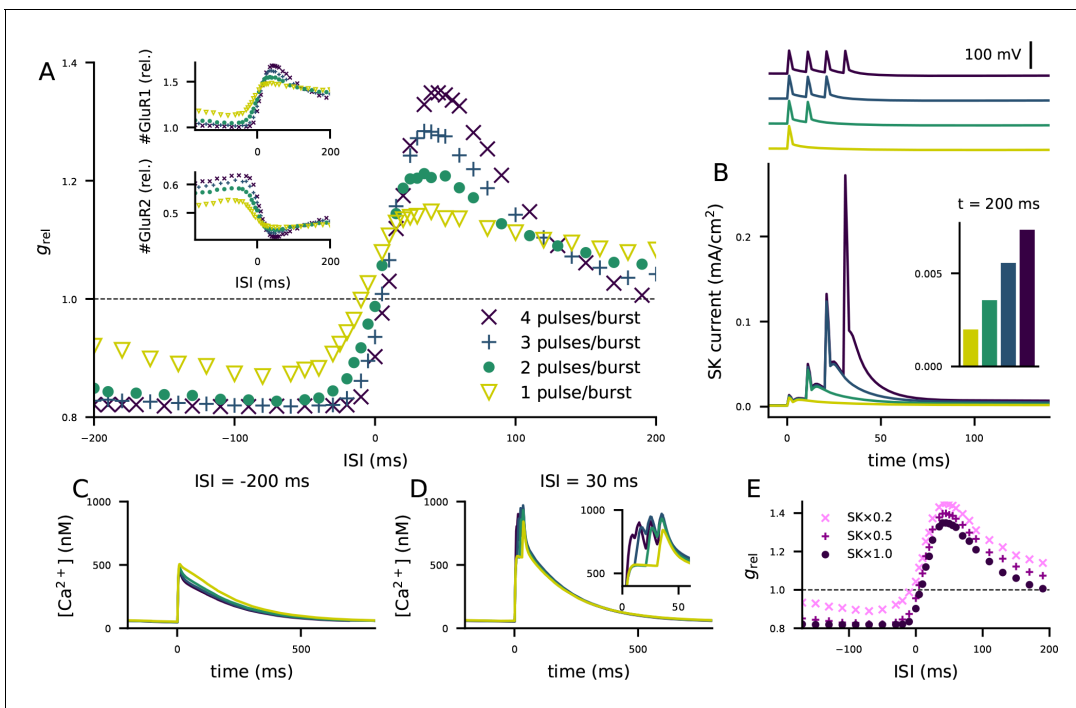


Figure 6. The STDP curve of layer 2/3 pyramidal cells is affected by the number of post-synaptic stimulus pulses associated with the pre-synaptic input. (A) The STDP curves of **Figure 5M** when the number of spikes per post-synaptic burst was 1 (yellow), 2 (green), 3 (blue), or 4 (as in **Figure 5**; dark purple). Inset: relative concentrations of membrane-inserted GluR1 (top) or GluR2 (bottom) subunits — see **Figure 5K–L** for reference. (B) Top: somatic membrane potential time course (aligned according to the onset of the first stimulus) for different numbers of post-synaptic stimulus pulses. Bottom: somatic SK current-density time course in the four conditions. Inset: the SK current densities 200 ms after the onset of the first post-synaptic stimulus. (C–D) Ca^{2+} flux to the dendritic spine when the pre-synaptic stimulation onset is 200 ms after (C) or 30 ms before (D) the onset of the last post-synaptic stimulus. (E) The STDP curves of **Figure 5M** when the number of spikes per post-synaptic burst was four but the somatic SK conductance parameter was either normal (dark purple), 50% smaller (magenta), or 80% smaller (pink).

The online version of this article includes the following figure supplement(s) for figure 6:

Figure supplement 1. The post-STDP synaptic conductance is weakly correlated with the peak of the Ca^{2+} input but strongly correlated with the mean Ca^{2+} input during the inter-stimulus interval.

in larger amplitude of GluR1 insertion and GluR2 endocytosis, which yields a dampened LTD for post-pre ISIs and strengthened LTP for large pre-post ISIs (**Figure 6A**). These counter-intuitive effects can be explained by the accumulation of small-conductance K^+ (SK) conductance in the post-synaptic neuron: the larger the number of post-synaptic pulses in the pairing burst, the larger the SK currents (**Figure 6B**). The SK current decays slowly (matching the Ca^{2+} concentration decay), and remnants of the SK currents can be observed as long as 200 ms after the post-synaptic stimulus (**Figure 6B** inset). For large post-pre ISIs, the number of spikes per burst has little effect on the Ca^{2+} transients during the post-synaptic stimulation (**Figure 6C** inset), but the SK currents activated by a large number of spikes per burst contribute to significantly decrease the Ca^{2+} transient caused by the pre-synaptic stimulus during the decay period (**Figure 6C**). By contrast, for small pre-post intervals, the additional spikes in the post-synaptic stimulus significantly contribute to the Ca^{2+} transients (**Figure 6D**). To show that the effects of the number of spikes per post-synaptic burst are mediated by the SK current, we ran the simulation of **Figure 5J** using a partial to complete blockage of the SK currents in the biophysically detailed simulations of the layer 2/3 pyramidal cell. The paired-pulse protocol of **Figure 5M** (involving both β -adrenergic and cholinergic neuromodulation) caused an STDP in all cases, but decreasing the SK conductance shortened the post-pre LTD window and decreased the amplitude of LTD (**Figure 6E**). Similar effects were obtained with a decrease of Ca^{2+} -channel conductances (not shown), which is in agreement with the data of **Nevian and Sakmann, 2006**. Our model predictions also agree with the observation that the plasticity outcome is not determined by Ca^{2+} transient amplitude (**Nevian and Sakmann, 2006**), instead, our model suggests

that the total Ca^{2+} is a better predictor of the plasticity outcome: the correlation coefficient between the post-STDP synaptic conductance and the peak Ca^{2+} transient amplitude (see **Figure 5—figure supplement 1E**) was 0.53, while that between the post-STDP synaptic conductance and the mean Ca^{2+} input during the inter-stimulus interval (see **Figure 5—figure supplement 1F**) was 0.96 (**Figure 6—figure supplement 1**).

The model predicts multimodal, protein concentration- and neuromodulation-dependent rules of plasticity

Cortical neurons express a variety of forms of LTP/LTD depending on the brain region and cell type. In computational studies, neocortical plasticity is most typically described by simple rules according to which small-amplitude Ca^{2+} inputs lead to depression of the synapse whereas large-amplitude inputs lead to potentiation. Apart from a few examples **Castellani et al., 2001**; **d’Alcantara et al., 2003**; **Castellani et al., 2005**; **Honda et al., 2013**, these models typically do not describe the intracellular signalling machinery leading to the resulting plasticity **Holthoff et al., 2002**; **Karmarkar et al., 2002**; **Badoual et al., 2006**; **Cornelisse et al., 2007**; **Kubota and Kitajima, 2008**; **Urakubo et al., 2008**. Unlike biochemically detailed models, the simple models cannot be used to explore whether and how the prevalence of different plasticity-related proteins gives rise to various types of LTP/LTD or their impairments, which is an important question in the study of mental disorders with deficits in cortical plasticity. Here, we analysed the biochemical underpinnings of different types of plasticity rules using our unified model of cortical plasticity in order to predict the conditions for different forms of plasticity.

In a similar fashion to section ‘ Ca^{2+} activates multiple pathways that regulate the post-synaptic plasticity in cortical PCs’, we simulated our model of the post-synaptic spine when stimulated with a prolonged (5 min) square-pulse influx of Ca^{2+} and neuromodulators. We randomly altered the model parameters controlling the initial concentrations of different proteins, namely, the ratio of GluR1 to all GluR subunits (i.e., $\frac{[\text{GluR1}]_{\text{total}}}{[\text{GluR1}]_{\text{total}} + [\text{GluR2}]_{\text{total}}}$, from here on referred to as GluR1 ratio), the concentration of NCX (regulating the rate of Ca^{2+} decay from the spine), and the concentrations of PKA-pathway and PKC-pathway proteins (upstream of PKA and PKC). Alterations of the initial concentration of CaMKII (the only molecule in our model that exclusively affects the CaMKII pathway) had little effect in most domains of plasticity considered here (not shown), and thus, we omitted it in this analysis. We sampled these parameters from the following intervals: GluR1 ratio from the interval from 0 to 1 (keeping the total concentration of GluR subunits fixed at 540 nM), NCX concentration from the interval from 0 to twice the original value (2×0.54 mM), and the PKA and PKC-pathway factors f_{PKA} and f_{PKC} from the interval from 0 to 2 (see Materials and methods, section ‘Parameter alterations and model fitting’). We simulated the post-synaptic spine 150,000 times using different random values for these parameters under zero, low (50 particles/ms), medium (150 particles/ms), and high (250 particles/ms) levels of Ca^{2+} input.

We classified the parameter sets based on the total synaptic conductance 15 min after the onset of the stimulation with the high Ca^{2+} flux (250 particles/ms): the relative synaptic conductance varied between 0.16 and 5.92, and thus, we grouped the parameter sets to 16 classes using a bin size of 0.36 (**Figure 7A**). We then analysed the parameter distributions and their co-variations within these classes and how the different parameters affected the shape of the LTP/LTD curve within each class. A special subset of the LTP/LTD curves were the BCM-type plasticity curves, where either 50 or 150 particles/ms Ca^{2+} injection resulted in LTD and the 250 particles/ms resulted in LTP.

Our model with the standard protein concentrations (GluR1 ratio 0.5, $[\text{NCX}] = 0.54$ mM, $f_{\text{PKA}} = f_{\text{PKC}} = 1.0$) produced a BCM-type curve in class 6 (**Figure 7A**, black dashed curve). Classes 11–16 exhibited the strongest LTP, with large synaptic conductance for both 150 and 250 particles/ms Ca^{2+} injection, whereas classes 1 and 2 only exhibited LTD (**Figure 7A**). Classes 3–12 exhibited BCM-type of plasticity but the majority of the LTP/LTD curves were of non-BCM type in each class (**Figure 7A**).

Three parameters — the GluR1 ratio, NCX concentration and f_{PKA} , differed significantly across the 16 classes (**Figure 7B–D**). Low GluR1 ratio was needed for strong LTD and medium or high GluR1 ratio for strong LTP (**Figure 7B**). However, the strongest forms of LTP (classes 11–16) were induced only when GluR1 ratio was smaller than 1 (**Figure 7B**), because a very low number of GluR2 subunits implied that the synapse has many homomeric GluR1 tetramers at a basal state, and thus

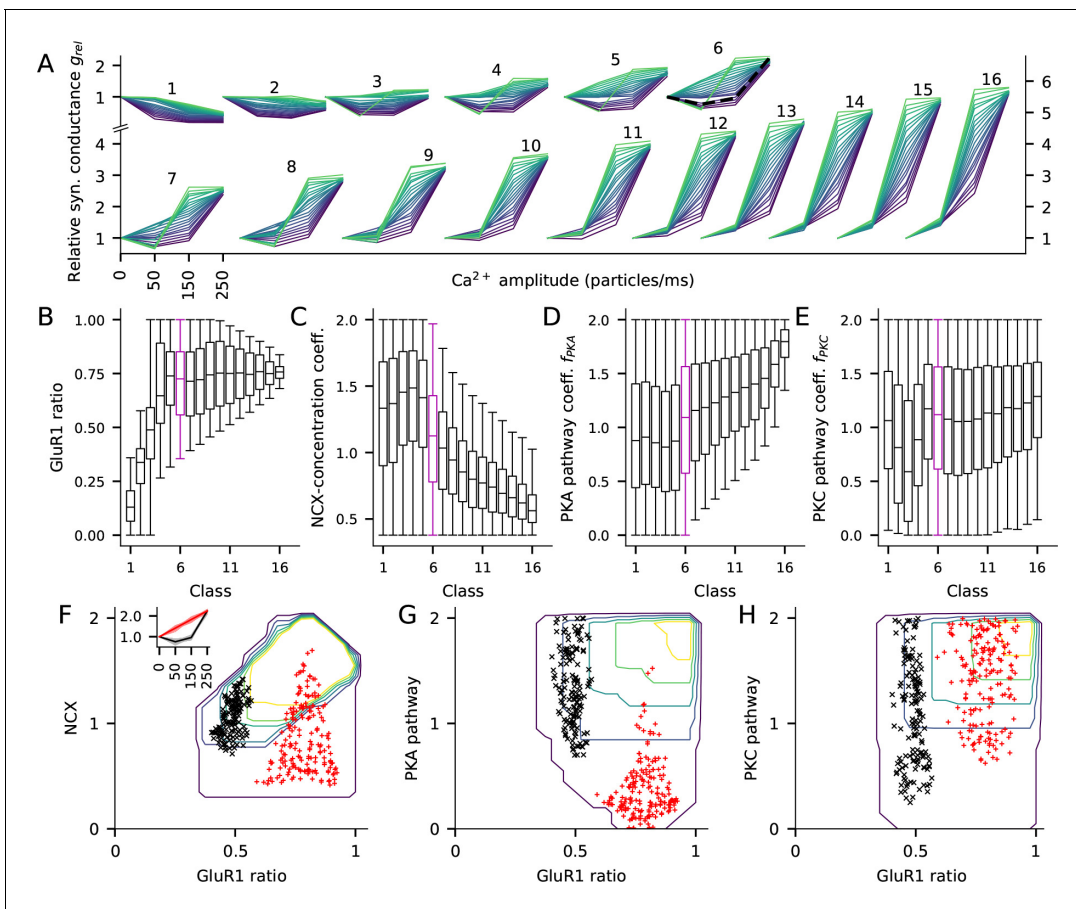


Figure 7. The fraction of GluR1s, number of Ca^{2+} extrusion proteins, and the concentrations of PKA and PKC-pathway proteins in the post-synaptic spine determine the type of LTP/LTD in the post-synaptic spine. (A) The LTP/LTD curves for all 16 classes. Four values of Ca^{2+} input amplitude were considered: 0, 50, 150, and 250 particles/ms (x-axis; repeated and overlaid for space). The y-axis shows the relative synaptic conductance, that is, total synaptic conductance 15 min after the onset of the Ca^{2+} input divided by the total synaptic conductance before the Ca^{2+} input. 20 representative parameter sets are displayed from each class, coloured from purple (lowest relative synaptic conductance response for medium Ca^{2+} input) to green (highest conductance). The black, dashed trace in class six represents the model with the default concentration parameters. (B–E) Distribution of model parameters, that is, GluR1 ratio (B), NCX-concentration coefficient (C), PKA pathway-concentration coefficient f_{PKA} (D), and PKC pathway-concentration coefficient f_{PKC} in the 16 classes. Class 6 (purple) highlighted for further analysis. F–H: GluR1 ratio plotted against NCX-concentration coefficient (F), f_{PKA} (G), and f_{PKC} (H) in class 6. The contours represent the distribution of parameters ($N = 5837$) that produced class-6 plasticity. No parameters yielding class-6 plasticity were found beyond the purple contour, and the inner contours cover the parameter space where the distribution is higher than 0%, 20%, 40%, 60% or 80% of the maximal density value. The black and red markers represent parameter sets that produced two plasticity subclasses, namely, one where the total deviance (summed absolute difference) from the BCM-type plasticity produced by the default parameter set (black, $N = 145$) or from a linearly increasing LTP (red, $N = 183$) was less than 0.2 (a.u.). The thick lines represent the centre of the subclasses (black: relative conductances in response to 50, 150, and 250 Ca^{2+} ions/ms: 1.41, 1.83, 2.24; red: relative conductances in response to 50, 150, and 250 Ca^{2+} ions/ms: 1.41, 1.83, 2.24). The online version of this article includes the following figure supplement(s) for figure 7:

Figure supplement 1. The PKC-pathway parameter distributions differ between clusters separated by their response to low (50 particles/ms) Ca^{2+} input.

stimulation-induced GluR1 exocytosis and GluR2 endocytosis did not radically increase the number of homomeric GluR1 tetramers (Equation 5, see also Figure 4D). For LTD and moderate LTP (classes 1–5), any NCX concentration and PKA-pathway coefficient could be used, but very strong LTP (classes 10–16) required a small to medium NCX concentration (Figure 7C) and a medium to large PKA-pathway coefficient (Figure 7D). By contrast, PKC-pathway coefficient alone was not predictive of plasticity outcome (Figure 7E).

The model results for the large parameter distributions of Figure 7B–E imply that there are manifestly different combinations of parameters that lead to the same LTP/LTD outcome. To analyse this

intrinsic variability, we studied the distributions of the model parameters within the class of moderate LTP (class 6, 132–168% LTP for 250 particles/ms; indicated by purple boxes in **Figure 7B–E**) in more detail. Dependencies among the four parameters could be observed in 2-dimensional contour plots of the parameter distributions (**Figure 7F–H**). With large (0.6) GluR1 ratios, any NCX, PKA or PKC concentration could be used, but with smaller (≤ 0.6) GluR1 ratios, smaller NCX concentration (**Figure 7F**) or larger PKA-pathway coefficients (**Figure 7G**) were needed to obtain class-6 type of plasticity. To illustrate how these parameters affect the shape of the plasticity curves within class 6, we plotted the parameter sets that produced a BCM-type LTP/LTD curve similar to the one produced by our default model (**Figure 7F** inset, black) or an LTP curve that was linear within this regime (**Figure 7F** inset, red). Moderate GluR1 ratios (0.40–0.57; **Figure 7F**, black) and moderate NCX concentrations (0.7–1.4 times the default value; **Figure 7F**, black) were needed for the default BCM-type plasticity, while for the linear LTP curve a larger GluR1 ratio (0.59–0.92; **Figure 7F**, red) was needed but the NCX concentration was more variable (values ranged from 0.4 to 1.7 times the default value; **Figure 7G**, red). The PKA pathway coefficients were generally larger in the default BCM-type plasticity parameter sets than in the parameter sets producing the linear LTP curve (**Figure 7G**). **Figure 7H** shows the distributions of a set of coefficients, i.e. the PKC pathway, which were not correlated with the plasticity outcome within this group.

Our previous analysis showed that PKC-pathway-mediated GluR2 endocytosis was important in lower stimulation frequency protocols (**Figure 3**) or in protocols with large separation between pre- and post-synaptic stimuli (**Figure 5**). To further analyze the contribution of PKC-pathway proteins to plasticity outcomes, we repeated the analysis of **Figure 7** by clustering the plasticity outcome based on the relative synaptic strength after a steady-state Ca^{2+} input of low amplitude (50 particles/ms; **Figure 7—figure supplement 1A**). As observed with the previous clustering, the GluR1 ratio and NCX concentration differed across classes (**Figure 7—figure supplement 1B and C**). However, in this classification, the PKA-pathway coefficient was not predictive of the plasticity outcome (**Figure 7—figure supplement 1D**) whereas the PKC-pathway coefficient varied across the classes (**Figure 7—figure supplement 1E**). Separation between BCM-like plasticity and gradual LTD was also evident within class 6', and due to the same GluR1, PKA and NCX parameters as with the original classification (**Figure 7—figure supplement 1F–H**). This shows our identification of critical parameters is robust to how the classification was performed.

Taken together, our results show that alterations of the concentrations of the proteins regulating Ca^{2+} efflux or PKA/PKC-pathway signalling and the numbers of GluR1 and GluR2 subunits, ranging from complete absence to moderate increase ($\pm 100\%$), have a large effect both on the type of plasticity (LTP or LTD) and on the sensitivity of the plasticity outcome to the amplitude of the Ca^{2+} flux. These data suggest that neocortical post-synaptic spines may exhibit a vast set of plasticity rules by downregulation or relatively mild upregulation of their protein expression.

A parametric analysis confirms the robustness of the model

We analysed the model responses to 4xHFS and LFS protocols (as in **Figure 3**) under small ($\pm 10\%$) changes in the parameters describing the initial concentrations and reaction rates (**Figure 8**). As expected, most parameter changes led to small deviations from the predicted magnitudes of LTP/LTD (**Figure 8**, grey bars). Alterations of the initial concentration of a number of species (10 out of 47) and reaction rates (12 out of 223) resulted in a notable ($>15\%$) amplification or attenuation of LTD (**Figure 8A**) or LTP (**Figure 8B**). The parameters affecting the LFS-induced LTD were all related to GluR1 membrane insertion or total amount of GluR1 or GluR2 (**Figure 8A**), while the parameters affecting the 4xHFS-induced LTP were related to NCX-mediated Ca^{2+} extrusion, PP1 concentration, production of cAMP by AC1, PKA buffering/deactivation, or GluR1 membrane insertion (**Figure 8B**). Importantly, none of the parameter changes completely abolished the LTP or LTD. Taken together, our model is robust to small alterations in initial concentrations and reaction rates, but parameters influencing the Ca^{2+} dynamics, GluR1 activity, or the PKA-pathway signalling can have relatively large effects on the model output.

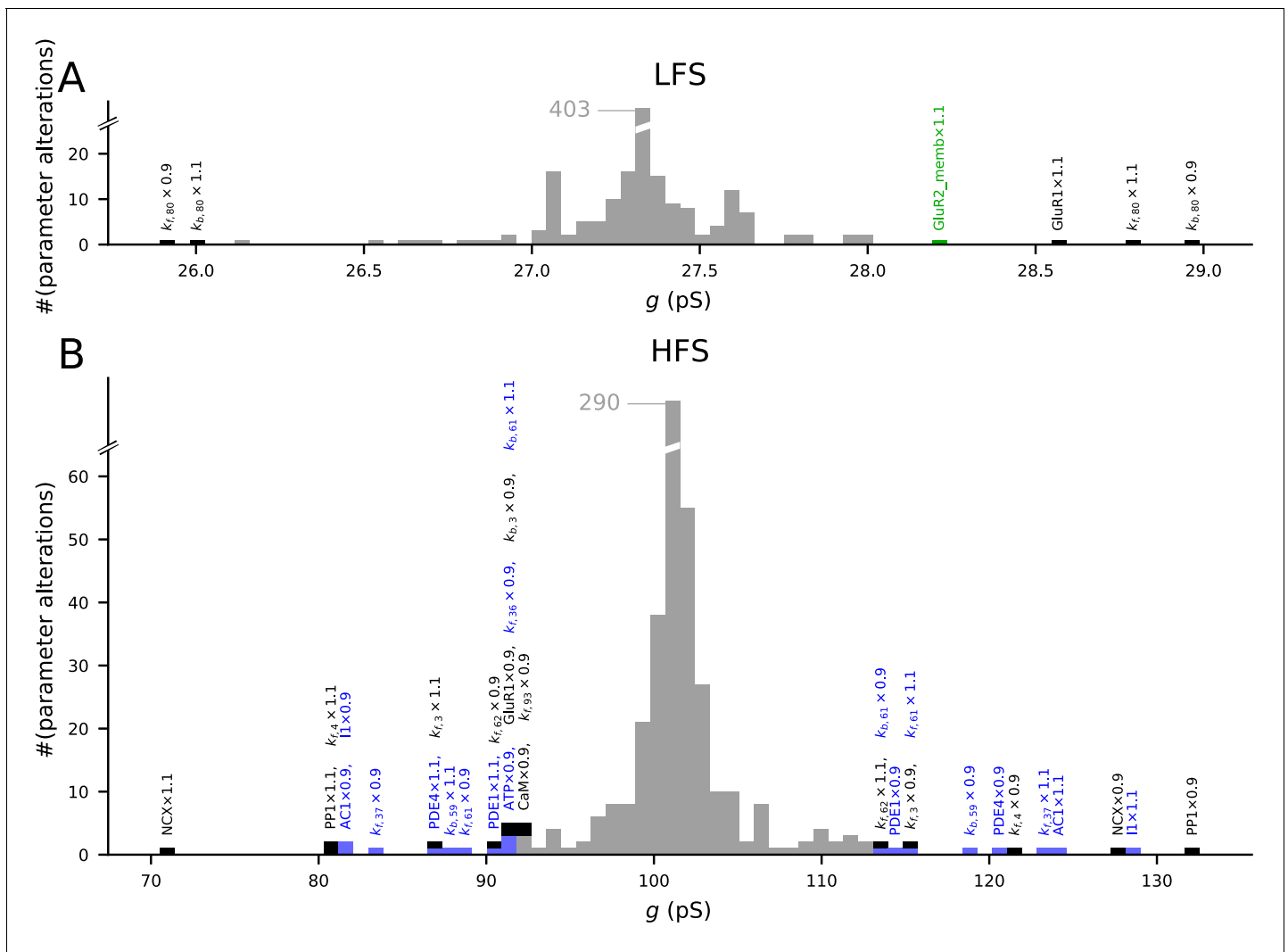


Figure 8. The model predictions of LTP and LTD are robust to small changes in model parameters. Values of initial concentrations (47 parameters) or reaction rates (223 parameters) were changed one at the time by -10% or $+10\%$, and the resulting synaptic conductance 16 min after LFS (A) or 4xHFS (B) protocol was measured (NEURON RxD simulations). The initial synaptic conductance is 33.4 pS (see **Figure 3A,S**), although some parameter changes mildly affected this value (data not shown). The x-axis shows the post-LFS (A) or post-HFS (B) synaptic conductance, and the y-axis shows the number of parameter alterations. Majority of the parameter changes had small effect on plasticity (grey bars), but changes in initial concentrations of 10 species and 12 reaction rates caused $>15\%$ change in the amplitude of LTP or LTD — these changes are represented by black (multi-pathway parameters), blue (PKA-pathway-related parameters), and green (PKC-pathway-related parameters) bars. The underlying parameter changes are printed above the corresponding bar.

The model flexibly reproduces data from various cortical LTP/LTD experiments

The richness of the intracellular signalling machinery behind LTP and LTD poses challenges for both qualitative and quantitative comparison between results from different cell types, obtained using different stimulation protocols, or even published by different laboratories *Larkman and Jack, 1995*. Computational biochemically detailed models have been proposed as an absolutely reproducible tool that is particularly suited for unifying our understanding of LTP and LTD across cell types and brain regions *Manninen et al., 2010*. Here, we show that our model for intracellular signalling in a cortical post-synaptic spine — through the use of varying concentrations of different proteins — can be flexibly tuned to reproduce data from the experimental literature of cortical LTP/LTD. This allows one to make predictions for the differences in intracellular machineries underlying each of the experiments, leading to a more complete view of the plasticity-related signalling pathways in

different cell types in the cortex and the effects of the stimulation protocol on the plasticity outcome across cortical areas.

To show the flexibility of our model, we aimed to reproduce a large amount of data on cortical plasticity across cortical areas and stimulation paradigms. We reviewed the literature of cortical

Table 2. List of LTP/LTD experiments in the cortex.

The first column labels the experimental data set and names the underlying study. The second column shows the considered synaptic pathway and the third column shows whether the observed LTP/LTD had a pre- or post-synaptic origin. The fourth and fifth columns show the frequency (in Hz) of stimulation and the number of pulses delivered, respectively: 10×4 means that 10 trains of 4 pulses with 10 ms interval (100 Hz) were delivered, and likewise, 25×5 means that 25 trains of 5 pulses with 10 ms interval were delivered. The sixth column tells whether the data were obtained in control conditions or under additional blockers or agonists. The seventh, eighth, ninth, and tenth columns show the relative change in synaptic strength 10, 15, and 20 min after the start of the stimulus protocol and an average SD of the relative synaptic strengths — these values were approximated from the LTP/LTD curves plotted in the underlying references. The rows correspond to experiments from a given reference that are divided to 11 different experimental data sets. Within each data set, the underlying system is assumed to be otherwise similar to the control except for the applied modifier: as an example, the chemical or genetic blockade of CaMKII activity (as performed in *Ma et al., 2008* and *Hardingham et al., 2003*) is here expected to only affect the ability of CaMKII to autophosphorylate, and the rest of the model parameters are kept fixed. The experiments printed in grey were included in the underlying study, but were excluded from the main analyses of the present work (see main text). EC – entorhinal cortex; PFC – prefrontal cortex; BC – barrel cortex; ACC – anterior cingulate cortex; VC – visual cortex; AuC – auditory cortex; CC – corpus callosum. (*): The LFS of 900 3-ms pulses at 5 Hz in data sets VC-1 and VC-2 was replaced by 180 15-ms pulses at 1 Hz to decrease computational load in the optimisation.

Data set	Reference	Pathway	Pre/post	Freq.	N _{pulses}	Experiment	10 min	15 min	20 min	SD	
EC-1	<i>Ma et al., 2008</i>	horizontal	mostly	100	100	control	1.3	1.4	1.3	0.1	
			post			CaMKII blocked	1.05	1.02	0.95	0.07	
						without post-syn. Ca ²⁺	1.05	1.05	1.1	0.09	
EC-2	<i>Ma et al., 2008</i>	ascending	mostly	100	100	control	1.6	1.6	1.6	0.11	
			post			PKA blocked	1.4	1.4	1.4	0.13	
						without post-syn. Ca ²⁺	1.3	1.4	1.4	0.13	
PFC-1	<i>Sáez-Briones et al., 2015</i>	CC→PFC	n/a	312	156	control	2.0	1.98	1.9	0.08	
							without β -adrenergic ligand	1.34	1.4	1.36	0.09
PFC-2	<i>Flores et al., 2011</i>	CC→PFC	n/a	312	156	control	1.7	1.6	1.64	0.12	
							without β -1-receptor agonist	1.43	1.45	1.43	0.1
BC	<i>Hardingham et al., 2003</i>	L4→L2/3	n/a	5	10 × 4	control	1.35	1.4	1.3	0.09	
							CaMKII mutant	1.25	1.2	1.1	0.09
ACC	<i>Song et al., 2017</i>	L5/6 → L2/3	post	5	10 × 4	control	1.55	1.4	1.4	0.05	
							without s845	1.1	1.05	1.05	0.07
							without s831	1.35	1.4	1.3	0.1
PFC-3	<i>Zhou et al., 2013</i>	L2/3 → L2/3	mostly	0.1	50	control	1.3	1.4	1.4	0.14	
			post			without β -1-receptor agonist	1.1	1.2	1.2	0.13	
VC-1 (adult)	<i>Kirkwood et al., 1997</i>	L4 → L3	n/a	5	10 × 4	(CTR, HFS)	1.3	1.26	1.26	0.07	
							(without CaMKII, HFS)	1.02	1.02	1.02	0.02
							(CTR, LFS)	n/a	0.95	0.95	0.05
							(without CaMKII, LFS)	n/a	0.88	0.93	0.03
VC-2 (4–5 w)	<i>Kirkwood et al., 1997</i>	L4 → L3	n/a	5	10 × 4	(CTR, HFS)	1.2	1.18	1.18	0.05	
							(without CaMKII, HFS)	1.07	1.09	1.08	0.03
							(CTR, LFS)	n/a	0.79	0.82	0.03
							(without CaMKII, LFS)	n/a	0.82	0.89	0.03
AuC-1	<i>Kotak et al., 2007</i>	L6 → L5	n/a	1	25 × 5	LTP-expressing cells	1.98	1.58	1.93	0.19	
AuC-2	<i>Kotak et al., 2007</i>	L6 → L5	n/a	1	25 × 5	LTD-expressing cells	0.77	0.68	0.67	0.09	

plasticity, and picked eight studies where one or more types of neurons were tested using one or more stimulation protocols and the outcome was quantified using electrophysiological measurements (**Table 2**). These studies comprised 11 data sets that described the response of a neuron population in entorhinal cortex (EC), prefrontal cortex (PFC), barrel cortex (BC), anterior cingulate cortex (ACC), visual cortex (VC), or auditory cortex (AuC) to plasticity inducing protocols (**Table 2**). For each experiment in each data set, we assigned an objective function that quantified the error between the predicted LTP/LTD outcome (measured in relative synaptic conductance) and the data (typically measured in fold change of field EPSP slope). The objective functions were averaged across different time instants (10, 15, and 20 min post-stimulus-onset). We then ran a multi-objective optimisation algorithm (see Materials and methods, section 'Parameter alterations and model fitting') that aimed at finding the values for model parameters that minimised these objective functions. The fitted parameters included the amplitudes of pre-synaptic stimulation-associated fluxes of Ca^{2+} , β -adrenergic ligand and glutamate in addition to GluR1 fraction and factors for the protein concentrations of different pathways. Here, both the Ca^{2+} and the neuromodulatory inputs were square-pulse injections that followed every pre-synaptic stimulation although some of the studies of **Table 2** used bath application of neuromodulatory agents; however, the temporal distribution of the neuromodulators has only a small effect in our model as shown earlier (**Figure 3—figure supplement 4**). We ran the optimiser for 20 generations. For data sets VC-1 and VC-2, we did not find parameter sets that would fulfil all four objective functions, and therefore, we re-fitted the model for these data sets excluding the CaMKII-blocked experiments (printed in grey in **Table 2**).

We found groups of parameter sets that fit within one standard deviation (SD) on average from the target values of synaptic conductance for each data set of **Table 2** (**Figure 9A–C**). There were differences in the numbers of acceptable parameter sets between the data sets due to differences in the postulated strength of the LTP/LTD, the number of experiments, and the SD of the post-stimulus synaptic conductance (**Figure 9D**). The data sets EC-1 and BC were particularly challenging to fit (<0.2% of the parameter sets tested by the optimiser gave an acceptable fit; **Figure 9D**). By contrast, the data set AuC-2 was the easiest to fit (3.9% of the parameter sets were acceptable; **Figure 9D**).

The obtained parameters reflect the pathways needed for the type of plasticity. For example, the LTP of synapses of the horizontal but not those of the ascending pathway to EC were blocked by CaMKII inhibition, while the LTP of synapses of the ascending pathway were blocked by PKA inhibition (**Ma et al., 2008**). This is reflected in the obtained parameter sets: the parameter controlling CaM and CaMKII concentrations (f_{CaMKII}) was significantly larger (U-test, p -value < 0.001) in the horizontal-pathway (data set EC-1) synapse models, while the parameter controlling upstream PKA-pathway proteins (f_{PKA}) was significantly larger in the models reproducing the data from the ascending pathway (data set EC-2; **Figure 9E**). The GluR1-GluR2 ratio, in turn, was not significantly different between the two data sets (**Figure 9E**). As a contrasting example, our model predicts a large variety of parameters that reproduce the LTP and LTD of data sets AuC-1 and AuC-2 but, consistent with the results of **Figure 7**, the GluR1 ratio was significantly larger in the model parameters fitted to the data from LTP-expressing neurons than from LTD-expressing neurons (**Figure 9E**). The complete graphs of parameter value distributions in the 11 data sets and the parameter set producing the best fit (**Figure 9A**) for each data set are shown in Supplementary data, **Figure 9—figure supplements 1–11**. Taken together, our model-fitting experiment shows that the model can be fit to many types of multi-condition plasticity data — without altering the reaction rates — and that the resulting predictions of the underlying protein concentrations reflect the mechanisms proposed by the experimental studies.

The models obtained by fitting the initial concentrations to data provide an important tool for predicting the outcome of plasticity under various stimulus protocols and chemical agents. We carried out additional simulations with the obtained models using HFS protocol. The models fitted for data from EC (data sets EC-1 and EC-2, [**Ma et al., 2008**]), BC (**Hardingham et al., 2003**), ACC (**Song et al., 2017**), and LTP-expressing auditory cortical neurons (data set AuC-1, **Kotak et al., 2007**) predicted a steady increase in response to HFS, while models fitted for other cortical data predicted a mixture of LTP, LTD, and no change (**Figure 10A**). Furthermore, to obtain experimentally testable predictions for the dependency of the plasticity outcome in different cortical areas on the intracellular signalling, we simulated the models from each data set with the corresponding stimulus protocol with CaMKII, PKA, or PKC blockade. The inhibition of CaMKII impaired

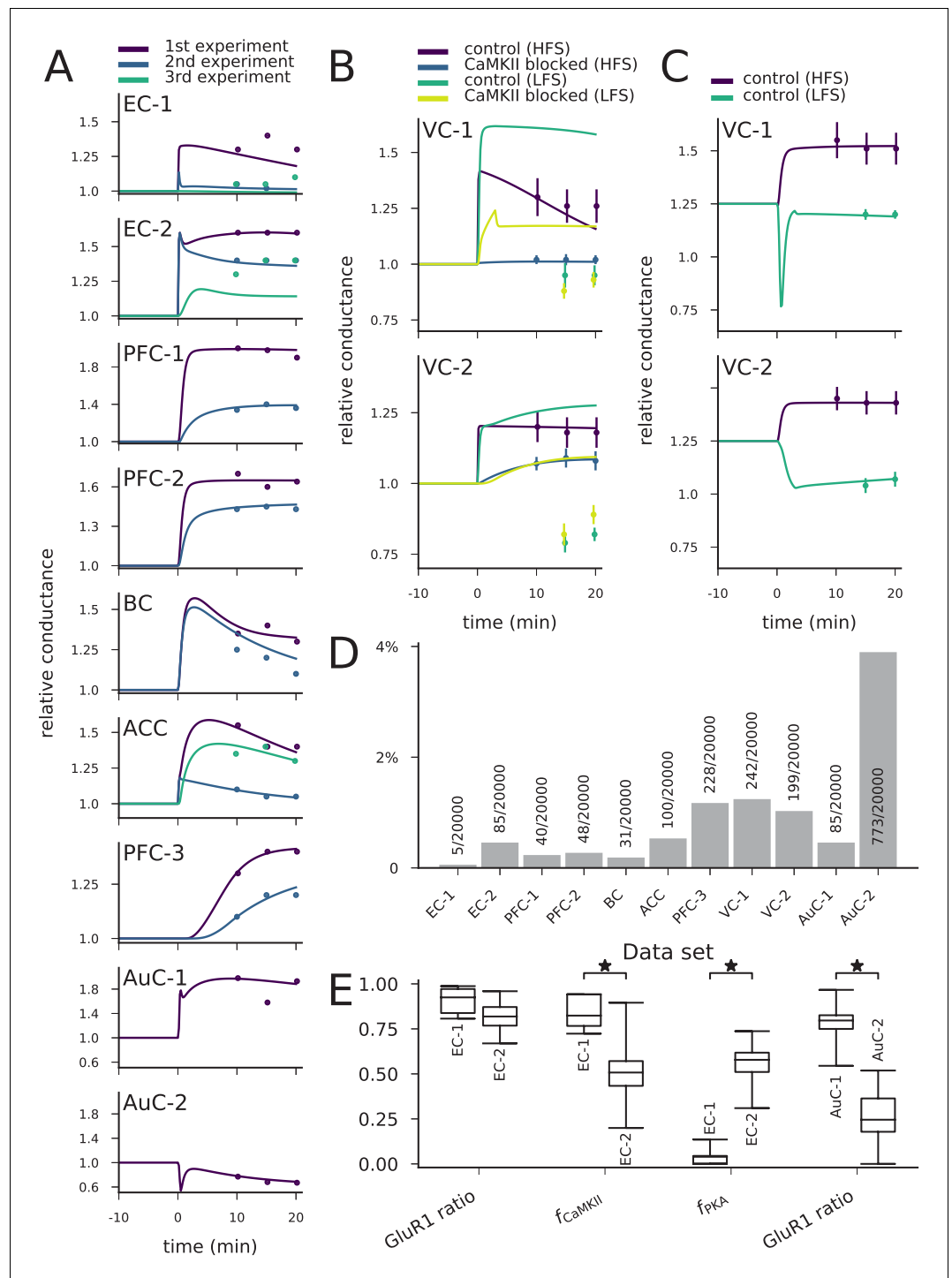


Figure 9. The model can be fit to LTP/LTD data from different cortical areas. (A) The model could be fit to LTP/LTD data from data sets EC-1 (top), EC-2, PFC-1, PFC-2, BC, ACC, PFC-3, AuC-1, and AuC-2 (bottom). The curves represent the model predictions of the best-fit parameter sets, and the dots represent the experimental data from **Table 2**. For data sets other than AuC-1 and AuC-2, several experiments with various chemical agents or genetic mutations were performed for each neuron population: these are ordered as in **Table 2** (e.g., in data set EC-1, purple (1st experiment) corresponds to control, blue (2nd experiment) to CaMKII-blocked experiment, and green (3rd experiment) to the experiment where post-synaptic Ca^{2+} was blocked). (B) The model could not be fit to the complete LTP/LTD data from data sets VC-1 (top) and VC-2 (bottom). The best parameter sets correctly predicted the LTP/LTD in up to two experiments (e.g., the selected parameter sets reproduce the HFS data with and without *Figure 9 continued on next page*

Figure 9 continued

CaMKII inhibitor, but failed to reproduce the LFS data). (C) The model could be fit to the LTP/LTD data from data sets VC-1 (top) and VC-2 (bottom) when CaMKII-blocked experiments were ignored. The vertical bars in (B) and (C) represent the SD from the experimental data. (D) Proportion of accepted parameter sets across the 20 generations of multi-objective optimisation (20'000 parameter sets in total) in each data set. (E) Box plots of selected parameters in the acceptable parameter sets of data sets EC-1 and EC-2 (three left-most pairs) and AuC-1 and AuC-2 (right-most pair). Values of f_{CaMKII} and f_{PKA} are linearly scaled such that the values 0 and 1 correspond to 0 and double the original value of the underlying parameters, respectively (CaM and CaMKII for f_{CaMKII} , and R, Gs, AC1, and AC8 for f_{PKA} , see Materials and methods, section 'Parameter alterations and model fitting'). The medians were significantly different in the compared data sets (U-test, p-value < 0.001).

The online version of this article includes the following figure supplement(s) for figure 9:

Figure supplement 1. Parameters for data set EC-1.

Figure supplement 2. Parameters for data set EC-2.

Figure supplement 3. Parameters for data set PFC-1.

Figure supplement 4. Parameters for data set PFC-2.

Figure supplement 5. Parameters for data set BC.

Figure supplement 6. Parameters for data set ACC.

Figure supplement 7. Parameters for data set PFC-3.

Figure supplement 8. Parameters for data set VC-1.

Figure supplement 9. Parameters for data set VC-2.

Figure supplement 10. Parameters for data set AC-1.

Figure supplement 11. Parameters for data set AC-2.

the LTP in data set EC-1 (horizontal pathway) but had little or no effect on the plasticity in other cortical areas (**Figure 10B**). The lack of effect of CaMKII blockade on the ascending pathway of EC — an experiment which was not included in the fitting of the model (**Table 2**) — validates the underlying models in this aspect since similar results were observed in *Ma et al., 2008*. Moreover, the similarities in the predicted effect of CaMKII-, PKA-, and PKC-pathway blockades between the two models of CC→PFC synapses (PFC-1 and PFC-2; **Figure 10B–D**) serve as an additional validation of these models. The inhibition of PKA impaired LTP in all cortical areas, except for LTP in the horizontal pathway of the EC (EC-1; **Figure 10C**). Our models also predicted that LTP of the CC→PFC pathway and LFS-induced LTP in VC can be effectively weakened or even be transformed to a mild LTD by PKA blockade (**Figure 10C**). Finally, our models predicted that PKC inhibition transformed all forms of LTD (LFS-induced LTD in VC-1 and VC-2; LTD in AuC-2) into LTP and impaired certain forms of LTP (LTP in EC-2; LTP in AuC-1) (**Figure 10D**). Taken together, our results suggest that almost all forms of post-synaptic plasticity in the cortex are likely to be PKA-dependent, and that many types of cortical plasticity are also influenced by CaMKII and PKC activity. Our results highlight the need for additional chemical or genetic manipulations to be done when experimenting on cortical plasticity in order to correctly reveal the intracellular signalling cascades in the post-synaptic spine.

Discussion

We built a single-compartment model describing the major post-synaptic signalling pathways leading to LTP and LTD in the cortex. We showed that our model reproduced conventional types of LTP and LTD, where an HFS-induced increase in GluR1 can increase the synaptic conductance (LTP) and an LFS-induced endocytosis of GluR2 can decrease it (LTD; **Figure 3**) and reproduced STDP data from visual cortical layer 2/3 pyramidal cells (**Figure 5**). Our model explains how different forms of plasticity depend on the concentrations of PKA- and PKC-pathway proteins (**Figure 7**). We also showed that our model can be fit to explain the pathway dependencies of various types of neocortical LTP/LTD data published in the literature by altering the magnitude of Ca^{2+} and ligand fluxes and the concentrations of post-synaptic proteins regulating the Ca^{2+} efflux and PKA- and PKC-pathway dynamics (**Figure 9**). Our fitted models provide a powerful tool for testing hypotheses on the effects of chemical or genetic manipulations on the LTP and LTD in different cortical regions (**Figure 10**).

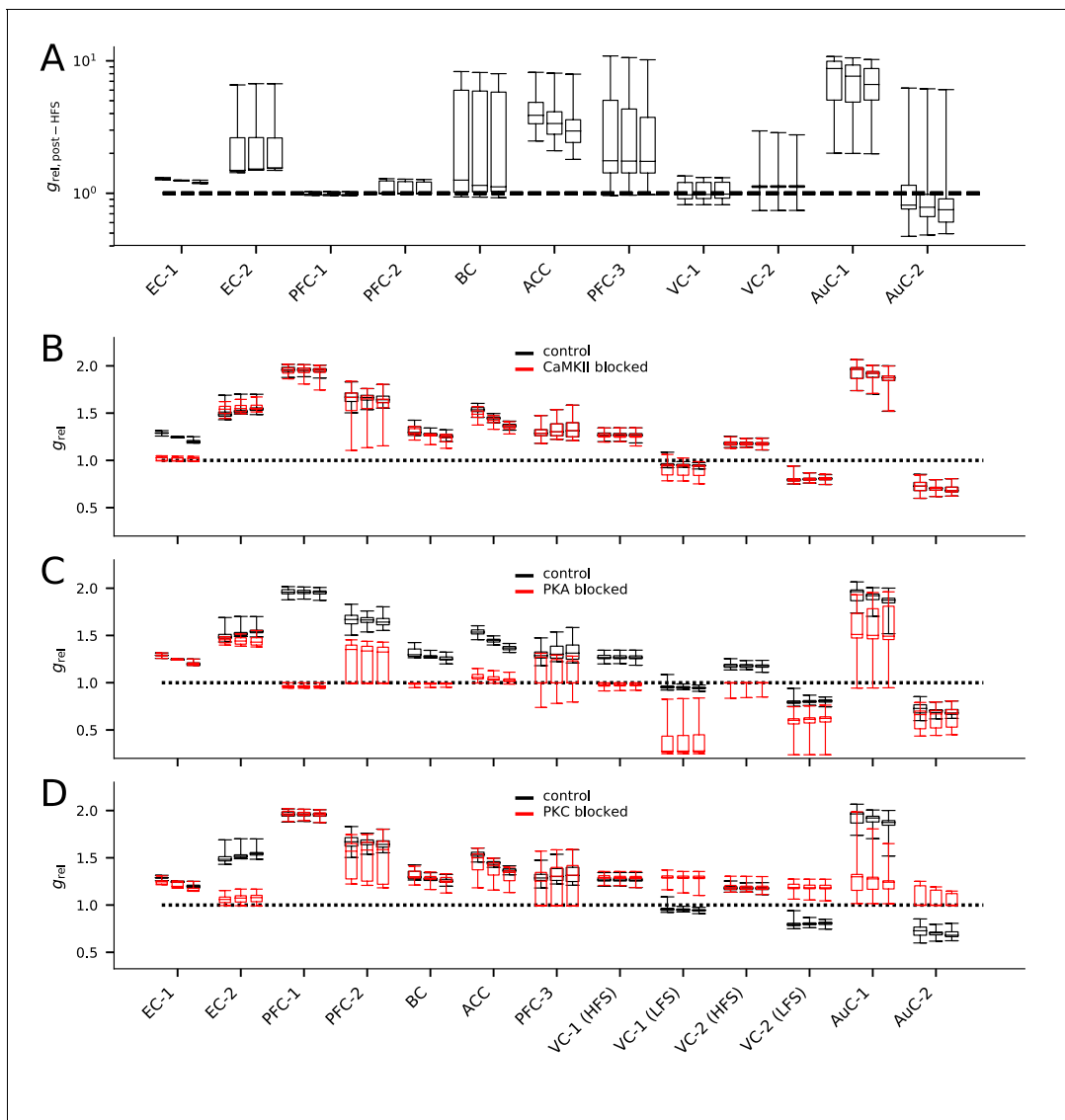


Figure 10. The models describing plasticity in different cortical areas predict diverse responses to modified stimulation protocol and stimulation under chemical blockers. (A) The predicted responses of the 20 best models in each data set to HFS (100 pulses at 100 Hz) stimulation. (B–D) The predicted responses of the 20 best models in each data set to the applied stimulation protocol (see [Table 2](#)) when CaMKII (B), PKA (C), or PKC (D) activity was blocked (red) or under control condition (black).

Role of GluR2 in synaptic plasticity in the neocortex

GluR2 subunits are highly expressed in neocortical neurons ([Kondo et al., 1997](#)), and their endocytosis mediates (or, at minimum, is correlated with) synaptic depression in many cortical regions such as ACC ([Toyoda et al., 2007](#)), VC ([Heynen et al., 2003](#)), and PFC ([Van den Oever et al., 2008](#)). Previous intracellular signalling-based models of neocortical LTP/LTD exist, but they do not take into account the contributions of GluR2 subunit. For example, in three previous models ([D'Alcantara et al., 2003](#); [Castellani et al., 2005](#); [Honda et al., 2013](#)), S831-phosphorylation-mediated LTP was described in a fashion similar to our model (although more approximations were made), but the phosphorylation site S845 was assumed to be basally phosphorylated and LTD was caused by modest Ca^{2+} inputs that led to PP1 or PP2B-mediated dephosphorylation of S845. Although there is support for this order of events ([Lee and Kirkwood, 2011](#); [Diering et al., 2016](#)), newer findings have confirmed the low degrees of phosphorylation of both S831 and S845 at a basal state in cortical cells, especially in synaptic spines ([Diering et al., 2016](#)). A recent phenomenological model has also shed light on the dependency of cortical STDP on the pairing interval and location of

the synapse (Ebner et al., 2019), but their mechanisms are not specific to any particular AMPAR or NMDAR subunit. To analyse the contributions of GluR2 subunits to neocortical LTP/LTD, we included in our model the signalling pathways leading to both phosphorylation-mediated exocytosis of GluR1 and endocytosis of GluR2. Our model could thus be used to study not only PKA-mediated LTP or PKC-mediated LTD but also their co-effects and co-dependencies.

Implications of the study

The modelling results of the present work give rise to experimentally testable predictions. For example, our STDP model, when stimulated without β -adrenergic ligands, suggests that at near-zero pairing-intervals the magnitude of the depression may be decreased or even switched to mild LTP (Figure 5J). In many experimental studies (including Seol et al., 2007), the type and magnitude of plasticity in this regime of STDP is not reported. We also predict that a mild LTP (24–60% LTP; class 4 in Figure 7) can be obtained through many differently weighted interactions of PKA and PKC pathways and Ca^{2+} extrusion strengths (Figure 7F–H, Figure 9—figure supplement 1 and 2, Figure 9—figure supplement 5–7). Importantly, this is the regime of a wealth of experimental LTP data (Tsumoto, 1990; Table 2), which is consistent with the great diversity of LTP mechanisms observed in the neocortex (Feldman, 2009). Based on our simulated data (Figure 10), we suggest that in order to correctly characterise the mechanisms behind LTP of especially this magnitude, both experiments that activate the PKA pathway and experiments that block or activate the PKC pathway should be carried out. It is also important to know whether and to what degree GluR1 and GluR2 subunits are present in the synapse, since the balance of GluR1 and GluR2 subunits seems to be a determinant parameter permitting certain types of plasticity while prohibiting others (Figures 7B and 9E, and Figure 3—figure supplement 1).

A key challenge in the study of synaptic plasticity is the diversity of LTP/LTD observed across the cell types in the brain (Granger and Nicoll, 2014). Differences in the transcriptome have been proposed as one of the sources for this variability (Lisachev and Shtark, 2018). We believe our model can be used to explain some of the discrepancies in the experimental data in this regard and expand the understanding of possible molecular contributors to LTP/LTD. For example, it is known that activation of PKA pathway by dopamine or noradrenaline in PFC pyramidal neurons increases the synaptic conductance through GluR1 membrane insertion (Sun et al., 2005; Xu et al., 2010). Our model is in agreement with this (Figure 3), but it also proposes that the LTP can be impaired by over- or underexpression of many involved proteins, such as AC1, I-1 (inhibitor of PP1), PDE4, PDE1, GluR1, and CaM, and even alterations in ATP concentration (see Figure 8B). Small differences in the concentrations of a number of such contributing proteins are likely to cause significant alterations to LTP observed in different brain areas and cell types.

Due to the inclusion of three major LTP/LTD pathways in the neocortex, our model provides a more accurate means than earlier models for exploring how the Ca^{2+} dynamics in the spine affects the plasticity outcome in many stimulation protocols, STDP in particular. Our model suggests that the plasticity outcome of the STDP protocol is strongly correlated with the total amount of Ca^{2+} entering the post-synaptic spine, and less so with the peak Ca^{2+} flux (Figure 6—figure supplement 1). The total amount of Ca^{2+} influx could thus provide a better biomarker for plasticity than the previously considered amplitude and duration of the Ca^{2+} transient (Evans and Blackwell, 2015).

Validity of the results and limitations of the study

Our model of total synaptic conductance of the post-synaptic spine is based upon a number of assumptions. First, the prediction of a large increase of conductance that follows the replacement of GluR2 subunits at the membrane by GluR1 subunits (e.g., Figure 3) is based upon the findings on differences in single-channel conductances of different types of AMPAR tetramers in hippocampal neurons (Oh and Derkach, 2005). Following Oh and Derkach, 2005, we assumed that CaMKII-phosphorylation of S831 only increases the conductance of GluR1 homomers and not that of GluR1/GluR2 heteromers, although also heteromers have been observed to increase their conductance in the presence of transmembrane AMPAR regulatory proteins (Kristensen et al., 2011). Second, we assumed a random tetramerization procedure in which each of the four subunits in the tetramer may be either GluR1 or GluR2 subunit. Traditionally, AMPARs were thought to assemble as dimers of like dimers, that is, that first GluR1s and GluR2s assemble into homomeric R1-R1 and R2-R2 dimers and

R1-R2 heterodimers and that these three types of dimers only assemble into tetramers with a dimer of its own kind (Gan et al., 2015). However, recent findings of heterotetramers with only one GluR1 subunit (Zhao et al., 2019) challenge this model. To show that our results were not dependent on the details of this process, we reproduced our results using the alternative (dimer of like dimers) tetramer formation rule. Using a slightly modified GluR1-GluR2 balance (35:65), this model reproduced HFS-induced LTP and LFS-induced LTD (Figure 3—figure supplement 2A) as well as the neuromodulator-gated STDP (Figure 3—figure supplement 2A). In summary, our model predictions were not dependent on the assumptions on the tetramer formation rule.

Our model reproduced the qualitative results of STDP of layer 2/3 pyramidal cells in visual cortex being gated by neuromodulators, but there were quantitative differences. When acetylcholine was present, our model predicted a prominent decrease in GluR2 membrane-expression regardless the pairing interval (Figure 5I), which caused a notable LTD for very large pairing intervals (Figure 5J), whereas the experimental data showed attenuation of the depression for large inter-stimulus intervals (Seol et al., 2007). This discrepancy is likely caused by processes allowing slower time-scale (>50 ms) interaction between the pre- and post-synaptic stimulus that are either not included (e.g., Ca^{2+} -induced Ca^{2+} release or cAMP-dependence of HCN channels) or not adequately strong in the multi-compartmental model. For example, the contributions of voltage-gated Ca^{2+} channels and SK channels to the neuron electrophysiology may be large (Mäki-Marttunen et al., 2017; Mäki-Marttunen et al., 2018) — to this end, we showed here that the SK currents are amplified by the subsequent pulses stimulating the post-synaptic neuron and that this is one factor increasing the LTD for large ISIs (Figure 6). Note that this prediction of lowered synaptic strength for large absolute ISIs is not to be considered a basal synaptic state under spontaneous activity since the amplitude of the LTD is significantly decreased both by the removal of cholinergic neuromodulation (Figure 6J) and a decrease of stimulating frequency (data not shown). On the other hand, mechanisms lacking from the biochemical model (e.g., voltage-dependence of the Ca^{2+} -extrusion rate of NCX Weber et al., 2002) could also impede our results in this matter. Some aspects of cellular physiology could therefore be better represented if we incorporated both biochemical signalling and multicompartmental Hodgkin-Huxley-type modelling into the simulations, as done in modelling studies of persistent neuron firing (Neymotin et al., 2016) and astrocyte electrophysiology (Savtchenko et al., 2018).

The quality of the model fitting to experimental data in Figure 9 is restricted by the fact that not all of the LTP/LTD data in Table 2 were confirmed to have a post-synaptic origin. This may be the key source of discrepancy in the fitting of the model to the CaMKII-blocked data from Kirkwood et al., 1997 (Figure 9B), since CaMKII activation at the pre-synaptic spine may lead to EPSC potentiation through an increase in neurotransmitter release (Ninan and Arancio, 2004). This scenario is supported by Seol et al., 2007 where S831-deficient mice were observed to show normal post-synaptic LTP in the VC.

Outlook

Our results on interactions of the different pathways in post-synaptic spines including both GluR1 and GluR2 subunits provide valuable insights on the contributions of protein expression on the plasticity of the synapse. Previously, synaptic plasticity outcomes in the cortex have been conjectured to depend on the type of the post-synaptic cell type, in addition to the timing and frequency of the applied stimuli and dendritic filtering properties (Bi and Poo, 1998; Sjöström et al., 2001). Our model provides a way to analyse exactly which aspects of PKA-, PKC- and CaMKII-pathway signalling underlie these cell-type-dependent differences in synaptic plasticity. Combining our biochemically detailed model with biophysically detailed models from different cortical areas will provide models with better predictive power in the future. Moreover, our model can be used for initial testing of hypotheses concerning dysfunctions (including chemical and genetic manipulations) of many intracellular signalling proteins and their role in impairments of cortical synaptic plasticity. By altering the initial concentrations or reaction rates of various species according to disease-associated functional genetics data, the model can be used to provide insights into the disease mechanisms of mental disorders that express both genetic disposition of post-synaptic signalling pathways and plasticity-related phenotypes, such as schizophrenia (Devor et al., 2017).

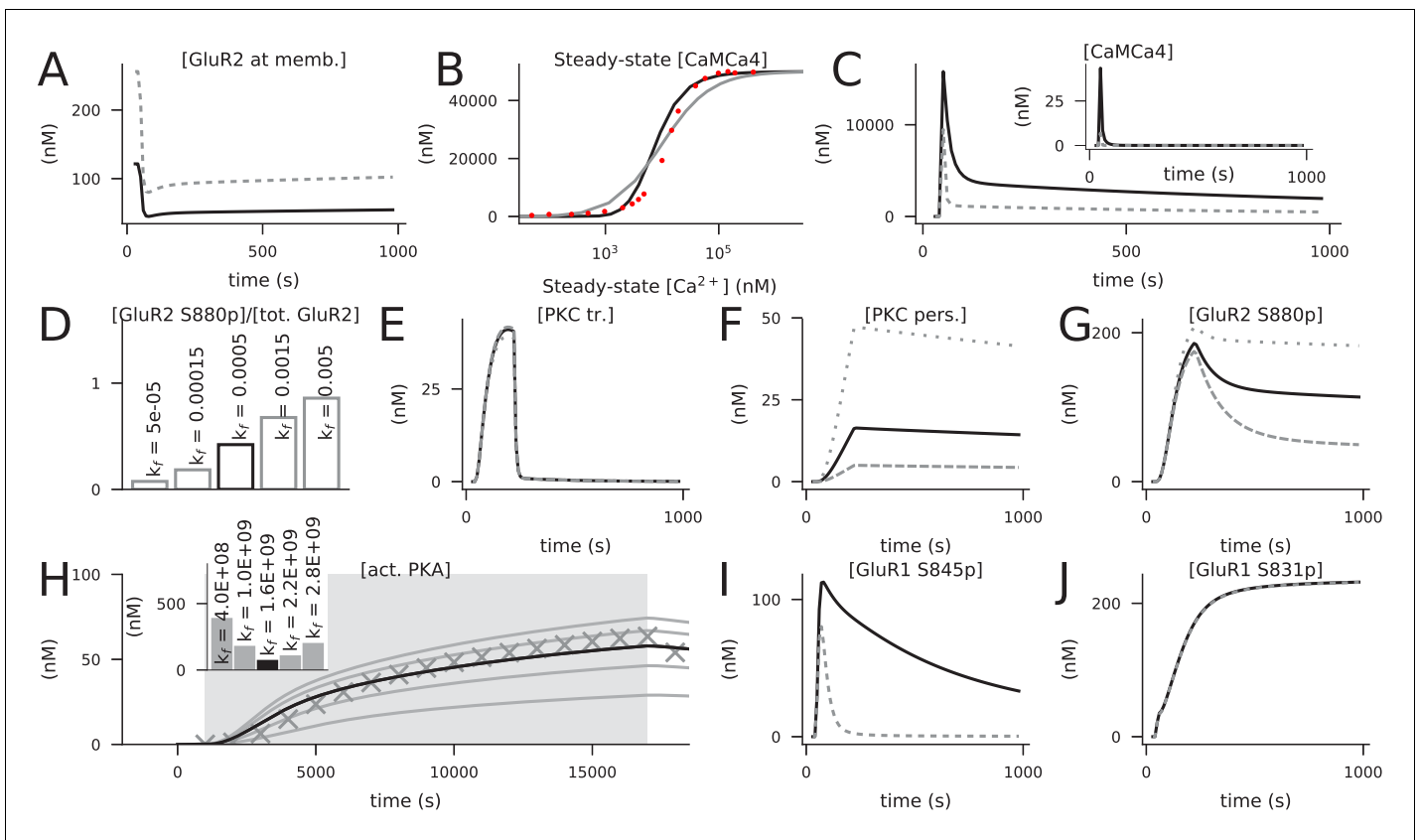


Figure 11. Calibration of the model. Black curves represent the final model, while grey lines represent predictions of models where previous model components or tentative parameter values were used. (A) Concentration of membrane-inserted GluR2 in 4xHFS when the forward rate of the membrane insertion of non-phosphorylated GluR2 was 0.0055 1/ms *Gallimore et al., 2018* (grey) or 0.00025 1/ms (black). The rate 0.00025 1/ms caused a resting-state concentration of 121 nM for the membrane-bound GluR2 subunits, which is 45% of the total GluR2 concentration (270 nM). (B) Steady-state concentration of activated (bound by four Ca^{2+} ions) CaM in response to a prolonged Ca^{2+} input amplitude when the two-step (grey) or three-step (black) activation of CaM by Ca^{2+} was used. The x-axis shows the corresponding steady-state concentration of free Ca^{2+} . Here, the initial concentrations of molecular species were as in *Li et al., 2020*, namely, 50 μM for CaM, Ng, PP2B, and CaMKII and 0 μM for all other species. Red dots show experimental data from *Hoffman et al., 2014*. (C) Concentration time course of non-protein-bound activated CaM (inset) or total activated CaM (main figure) in response to 4xHFS when the two-step (grey) or three-step (black) activation of CaM by Ca^{2+} was used. (D) Percentage of S880-phosphorylated GluR2 15 min after LFS when different forward rates of the activation of persistent PKC (k_f between 0.00005 and 0.005 1/(nM ms)) were used. The value $k_f = 0.0005$ 1/(nM ms) gave a percentage of 47%, in close agreement with *Ashby et al., 2004*. (E–G) The dynamics of transiently active PKC (E) were not strongly influenced by the forward rate of the activation of persistent PKC (reaction 140), but those of persistently active PKC (F) and S880-phosphorylated GluR2 (G) were significantly affected. Black curves show the data corresponding to $k_f = 0.00015$ 1/(nM ms) (dashed) and $k_f = 0.0015$ 1/(nM ms) (dotted), while the grey lines show the data corresponding to $k_f = 0.0005$ 1/(nM ms) (solid). (H) Predicted responses of an isolated PKA activation model (reactions 59 and 93) to a 16 s cAMP input (dim grey background) when different values of the forward rate of PKA binding with four cAMP molecules were used. The curves show the concentration of the catalytic PKA subunit when different forward rates of PKA–cAMP binding (from bottom to top: 0.4×10^9 , 1.0×10^9 , 1.6×10^9 , 2.2×10^9 , and 2.8×10^9 1/(nM⁴ms)) were used. The markers show the corresponding data when the two-step PKA–cAMP binding model of *Jędrzejewska-Szmek et al., 2017* was used. Inset: summed absolute differences between the tentative data (curves) and simulated data from the previous model (markers). The model with the forward rate of $k_f = 1.6 \times 10^9$ 1/(nM⁴ms) gave the closest correspondence to the model of *Jędrzejewska-Szmek et al., 2017*. (I) Concentration of S845-phosphorylated GluR1 in response to 4xHFS when the single-step (reaction 59, black) or two-step (from *Jędrzejewska-Szmek et al., 2017*, grey) PKA–cAMP binding was used. (J) Concentration of S831-phosphorylated GluR1 in response to 4xHFS when PKC did (black) or did not (grey, overlaid) phosphorylate S831 in GluR1s.

The online version of this article includes the following figure supplement(s) for figure 11:

Figure supplement 1. 1 hr of simulation without inputs is sufficient to obtain a steady state.

Figure supplement 2. The model STDP model is robust to changes in AMPA conductance but sensitive to changes in NMDA conductance in the multicompartmental layer 2/3 pyramidal cell model.

Table 3. List of model reactions.

(A) The reaction-rate units are in 1/ms, 1/(nMms), 1/(nM²ms), 1/(nM³ms), or 1/(nM⁴ms), depending on the number of reactants. Reactions are grouped by similar modes of action and identical forward and backward rates. The denominators **X**, **Y**, and **Z** represent groups of species detailed below. †: backward reaction rate proportional to [PKAc], not to [PKAc]². (B) Groups of species as used in panel (A).

(A)		Forw.	Backw.			Forw.	Backw.
ID	Reaction	Rate	Rate	ID	Reaction	Rate	Rate
1	Ca + PMCA \rightleftharpoons PMCACa	5e-05	0.007	71	GluR1 X ₂₂ + Y ₂₂ \rightleftharpoons GluR1 Z ₂₂	2.78e-08	0.002
2	PMCACa \rightleftharpoons PMCA + CaOut	0.0035	0.0	72	GluR1 X ₂₃ \rightleftharpoons GluR1 Y ₂₃ + Z ₂₃	0.0005	0
3	Ca + NCX \rightleftharpoons NCXCa	1.68e-05	0.0112	73	GluR1 X ₂₄ + PKAc \rightleftharpoons GluR1 Z ₂₄	4e-06	0.024
4	NCXCa \rightleftharpoons NCX + CaOut	0.0056	0.0	74	GluR1 X ₂₅ + PP1 \rightleftharpoons GluR1 Z ₂₅	8.7e-07	0.00068
5	CaOut + Leak \rightleftharpoons CaOutLeak	1.5e-06	0.0011	75	GluR1 X ₂₆ \rightleftharpoons GluR1 Y ₂₆ + PP1	0.00017	0
6	CaOutLeak \rightleftharpoons Ca + Leak	0.0011	0.0	76	GluR1 X ₂₇ + PP1 \rightleftharpoons GluR1 Z ₂₇	8.75e-07	0.0014
7	Ca + Calbin \rightleftharpoons CalbinC	2.8e-05	0.0196	77	GluR1 X ₂₈ \rightleftharpoons GluR1 Y ₂₈ + PP1	0.00035	0
8	L \rightleftharpoons LOut	0.0005	2e-09	78	GluR1 X ₂₉ + PP2BCaMCA4 \rightleftharpoons GluR1 Z ₂₉	2.01e-06	0.008
9	L + R \rightleftharpoons LR	5.555e-06	0.005	79	GluR1 X ₃₀ \rightleftharpoons GluR1 Y ₃₀ + PP2BCaMCA4	0.002	0
10	LR + Gs \rightleftharpoons LRGs	6e-07	1e-06	80	GluR1 X ₃₁ \rightleftharpoons GluR1_memb X ₃₁	2e-07	8e-07
11	Gs + R \rightleftharpoons GsR	4e-08	3e-07	81	GluR1_S845 X ₃₂		
12	GsR + L \rightleftharpoons LRGs	2.5e-06	0.0005		\rightleftharpoons GluR1_memb_S845 X ₃₂	3.28e-05	8e-06
13	LRGs \rightleftharpoons LRGsbg + GsaGTP	0.02	0.0	82	PDE1 + CaMCA4 \rightleftharpoons PDE1CaMCA4	0.0001	0.001
14	LRGsbg \rightleftharpoons LR + Gsbg	0.08	0.0	83	PDE1CaMCA4 + cAMP \rightleftharpoons PDE1CaMCA4cAMP	4.6e-06	0.044
15	X ₁ + PKAc \rightleftharpoons PKAc X ₁	8e-07	0.00448	84	PDE1CaMCA4cAMP \rightleftharpoons PDE1CaMCA4 + AMP	0.011	0.0
16	PKAc X ₂ \rightleftharpoons p X ₂ + PKAc	0.001	0.0	85	AMP \rightleftharpoons ATP	0.001	0.0
17	ppLR + PKAc \rightleftharpoons PKAcppLR	1.712e-05	0.00448	86	PDE4 + cAMP \rightleftharpoons PDE4cAMP	2.166e-05	0.0034656
18	pppLR + PKAc \rightleftharpoons PKAcpppLR	0.001712	0.00448	87	PDE4cAMP \rightleftharpoons PDE4 + AMP	0.017233	0.0
19	ppppLR + Gi \rightleftharpoons ppppLRGi	0.00015	0.00025	88	X ₃₃ + Y ₃₃ \rightleftharpoons PKAc Z ₃₃	2.5e-07	8e-05
20	ppppLRGi \rightleftharpoons ppppLRGibg + GiaGTP	0.000125	0.0	89	PKAc X ₃₄ \rightleftharpoons pPDE4 Y ₃₄ + PKAc	2e-05	0.0
21	pppp X ₃ \rightleftharpoons pppp Y ₃ + Gibg	0.001	0.0	90	pPDE4 \rightleftharpoons PDE4	2.5e-06	0.0
22	p X ₄ \rightleftharpoons X ₄	2.5e-06	0.0	91	pPDE4 + cAMP \rightleftharpoons pPDE4cAMP	0.000433175	0.069308
23	pp X ₅ \rightleftharpoons p X ₅	2.5e-06	0.0	92	pPDE4cAMP \rightleftharpoons pPDE4 + AMP	0.3446674	0.0
24	R + PKAc \rightleftharpoons PKAcR	4e-08	0.00448	93	PKAcAMP4 \rightleftharpoons PKAr + 2*PKAc	0.00024	2.55e-05
25	pR + PKAc \rightleftharpoons PKAcpR	4e-07	0.00448	94	Ca + fixedbuffer \rightleftharpoons fixedbufferCa	0.0004	20.0
26	ppR + PKAc \rightleftharpoons PKAcppR	4e-06	0.00448	95	Glu \rightleftharpoons GluOut	0.0005	2e-10
27	pppR + PKAc \rightleftharpoons PKAcpppR	0.0004	0.00448	96	Ca + PLC \rightleftharpoons PLCCa	4e-07	0.001
28	ppppR + Gi \rightleftharpoons ppppRGi	7.5e-05	0.000125	97	GqaGTP + PLC \rightleftharpoons PLCCGqaGTP	7e-07	0.0007
29	ppppRGi \rightleftharpoons ppppRGibg + GiaGTP	6.25e-05	0.0	98	Ca + PLCCGqaGTP \rightleftharpoons PLCCaGqaGTP	8e-05	0.04
30	GsaGTP \rightleftharpoons GsaGDP	0.01	0.0	99	GqaGTP + PLCCa \rightleftharpoons PLCCaGqaGTP	0.0001	0.01
31	GsaGDP + Gsbg \rightleftharpoons Gs	0.1	0.0	100	PLCCa + Pip2 \rightleftharpoons PLCCaPip2	3e-08	0.01
32	GiaGTP \rightleftharpoons GiaGDP	0.000125	0.0	101	PLCCaPip2 \rightleftharpoons PLCCaDAG + Ip3	0.0003	0.0
33	GiaGDP + Gibg \rightleftharpoons Gi	0.00125	0.0	102	PLCCaDAG \rightleftharpoons PLCCa + DAG	0.2	0.0
34	GsaGTP + AC1 \rightleftharpoons AC1GsaGTP	3.85e-05	0.01	103	PLCCaGqaGTP + Pip2 \rightleftharpoons PLCCaGqaGTPPip2	1.5e-05	0.075
35	AC1 X ₆ + CaMCA4 \rightleftharpoons AC1 Z ₆	6e-06	0.0009	104	PLCCaGqaGTPPip2 \rightleftharpoons PLCCaGqaGTPDAG + Ip3	0.25	0.0
36	X ₇ + ATP \rightleftharpoons Z ₇	1e-05	2.273	105	PLCCaGqaGTPDAG \rightleftharpoons PLCCaGqaGTP + DAG	1.0	0.0
37	AC1GsaGTPCaMCA4ATP			106	Ip3degrad + Plkinase \rightleftharpoons Ip3degPlk	2e-06	0.001
	\rightleftharpoons cAMP + AC1GsaGTPCaMCA4	0.02842	0.0	107	Ip3degPlk \rightleftharpoons Plkinase + Pip2	0.001	0.0
38	X ₈ + Y ₈ \rightleftharpoons AC1Gsa Z ₈	6.25e-05	0.01	108	PLC X ₃₅ \rightleftharpoons PLC Y ₃₅ + GqaGDP	0.012	0.0
39	X ₉ \rightleftharpoons cAMP + Z ₉	0.002842	0.0	109	GqaGTP \rightleftharpoons GqaGDP	0.001	0.0

Table 3 continued on next page

Table 3 continued

(A)				(B)			
ID	Reaction	Forw. Rate	Backw. Rate	ID	Reaction	Forw. Rate	Backw. Rate
40	AC1GiaGTPCaMCA4ATP \rightleftharpoons cAMP + AC1GiaGTPCaMCA4	0.0005684	0.0	110	GqaGDP \rightleftharpoons Gqabg	0.01	0.0
41	AC1CaMCA4ATP \rightleftharpoons cAMP + AC1CaMCA4	0.005684	0.0	111	Ca + DGL \rightleftharpoons CaDGL	0.000125	0.05
42	AC8 + CaMCA4 \rightleftharpoons AC8CaMCA4	1.25e-06	0.001	112	DAG + CaDGL \rightleftharpoons DAGCaDGL	5e-07	0.001
43	CaM + 2*Ca \rightleftharpoons CaMCA2	1.7e-08	0.035	113	DAGCaDGL \rightleftharpoons CaDGL + 2AG	0.00025	0.0
44	X_{10} + Ca \rightleftharpoons Z_{10}	1.4e-05	0.228	114	Ip3 \rightleftharpoons Ip3degrad	0.01	0.0
45	X_{11} + Ca \rightleftharpoons Z_{11}	2.6e-05	0.064	115	2AG \rightleftharpoons 2AGdegrad	0.005	0.0
46	CaM + Ng \rightleftharpoons NgCaM	2.8e-05	0.036	116	DAG + DAGK \rightleftharpoons DAGKdag	7e-08	0.0008
47	CaM + PP2B \rightleftharpoons PP2BCaM	4.6e-06	1.2e-06	117	DAGKdag \rightleftharpoons DAGK + PA	0.0002	0.0
48	CaMCA X_{12} + PP2B \rightleftharpoons PP2B Z_{12}	4.6e-05	1.2e-06	118	Ca + PKC \rightleftharpoons PKCCa	1.33e-05	0.05
49	PP2BCaM + 2*Ca \rightleftharpoons PP2BCaMCA2	1.7e-07	0.35	119	PKCCa + DAG \rightleftharpoons PKCt	1.5e-08	0.00015
50	CaMCA4 + CK \rightleftharpoons CKCaMCA4	1e-05	0.003	120	Glu + MGLuR \rightleftharpoons MGLuR_Glu	1.68e-08	0.0001
51	2*CKCaMCA4 \rightleftharpoons Complex	1e-07	0.01	121	MGLuR_Glu \rightleftharpoons MGLuR_Glu_desens	6.25e-05	1e-06
52	CKpCaMCA4 + CKCaMCA4 \rightleftharpoons pComplex	1e-07	0.01	122	Gqabg + MGLuR_Glu \rightleftharpoons MGLuR_Gqabg_Glu	9e-06	0.00136
53	CK X_{13} + Complex \rightleftharpoons CK X_{13} + pComplex	1e-07	0.0	123	MGLuR_Gqabg_Glu \rightleftharpoons GqaGTP + MGLuR_Glu	0.0015	0.0
54	2*Complex \rightleftharpoons Complex + pComplex	1e-05	0.0	124	GluR2 X_{36} + PKC Y_{36} \rightleftharpoons GluR2 Z_{36}	4e-07	0.0008
55	Complex + pComplex \rightleftharpoons 2*pComplex	3e-05	0.0	125	GluR2 X_{37} \rightleftharpoons GluR2 Y_{37} + PKC Z_{37}	0.0047	0
56	CKpCaMCA4 \rightleftharpoons CaMCA4 + CKp	8e-07	1e-05	126	GluR2 X_{38} + PP2A \rightleftharpoons GluR2 Z_{38}	5e-07	0.005
57	CKp X_{14} + PP1 \rightleftharpoons CKp Z_{14}	4e-09	0.00034	127	GluR2 X_{39} \rightleftharpoons GluR2 Y_{39} + PP2A	0.00015	0
58	CKp X_{15} \rightleftharpoons PP1 + CK Z_{15}	8.6e-05	0.0	128	GluR2 X_{40} \rightleftharpoons GluR2_memb X_{40}	0.00024545	0.0003
59	PKA + 4*cAMP \rightleftharpoons PKAcAMP4	1.6e-15	6e-05	129	GluR2_S880 X_{41} \rightleftharpoons GluR2_memb_S880 X_{41}	0.0055	0.07
60	Epac1 + cAMP \rightleftharpoons Epac1cAMP	3.1e-08	6.51e-05	130	ACh + M1R \rightleftharpoons AChM1R	9.5e-08	0.0025
61	I1 + PKAc \rightleftharpoons I1PKAc	1.4e-06	0.0056	131	Gqabg + AChM1R \rightleftharpoons AChM1RGq	2.4e-05	0.00042
62	I1PKAc \rightleftharpoons Ip35 + PKAc	0.0014	0.0	132	Gqabg + M1R \rightleftharpoons M1RGq	5.76e-07	0.00042
63	Ip35 + PP1 \rightleftharpoons Ip35PP1	1e-06	1.1e-06	133	ACh + M1RGq \rightleftharpoons AChM1RGq	3.96e-06	0.0025
64	Ip35 X_{16} + PP2BCaMCA4 \rightleftharpoons Ip35PP2B Z_{16}	9.625e-05	0.33	134	AChM1RGq \rightleftharpoons GqaGTP + AChM1R	0.0005	0.0
65	Ip35PP2B X_{17} \rightleftharpoons I1 + PP2B X_{17}	0.055	0.0	135	ACh \rightleftharpoons	0.006	0
66	PP1PP2BCaMCA4 \rightleftharpoons PP1 + PP2BCaMCA4	0.0015	0.0	136	Ca + PLA2 \rightleftharpoons CaPLA2	6e-07	0.003
67	GluR1 X_{18} + PKAc \rightleftharpoons GluR1 Z_{18}	4.02e-06	0.024	137	CaPLA2 + Pip2 \rightleftharpoons CaPLA2Pip2	2.2e-05	0.444
68	GluR1 X_{19} \rightleftharpoons GluR1 Y_{19} + PKAc	0.006	0	138	CaPLA2Pip2 \rightleftharpoons CaPLA2 + AA	0.111	0.0
69	GluR1 X_{20} + CK Y_{20} \rightleftharpoons GluR1 Z_{20}	2.224e-08	0.0016	139	AA \rightleftharpoons Pip2	0.001	0.0
70	GluR1 X_{21} \rightleftharpoons GluR1 Y_{21} + CK Z_{21}	0.0004	0	140	PKCt + AA \rightleftharpoons PKCp	5e-09	1.76e-07

$X_1 \in \{LR, pLR\}$	$(X_{23}, Y_{23}, Z_{23}) \in \{(_CKpCam, _S831, CKpCaMCA4), (_PKCt, _S831, PKCt), (_PKCp, _S831, PKCp), (_S845_CKpCam, _S845_S831, PKCt), (_S845_PKCp, _S845_S831, PKCt), (_S845_PKCp, _S845_S831, PKCp), (_memb_CKpCam, _memb_S831, CKpCaMCA4), (_memb_PKCt, _memb_S831, PKCt), (_memb_PKCp, _memb_S831, PKCp), (_memb_S845_CKpCam, _memb_S845_S831, CKpCaMCA4), (_memb_S845_PKCt, _memb_S845_S831, PKCt), (_memb_S845_PKCp, _memb_S845_S831, PKCt)\}$
$X_2 \in \{LR, pLR, ppLR, pppLR, R, pR, ppR, pppR\}$	
$(X_3, Y_3) \in \{(LRGibg, LR), (RGibg, R)\}$	
$X_4 \in \{LR, R, pR\}$	
$X_5 \in \{LR, pLR, ppLR, pR, ppR\}$	
$(X_6, Z_6) \in \{(GsaGTP, GsaGTPCaMCA4), (GsaGTPGsaGTP, GsaGTPGsaGTPCaMCA4), (\{ \}, CaMCA4)\}$	

Table 3 continued on next page

Table 3 continued

(B)

$(\mathbf{X}_7, \mathbf{Z}_7) \in \{ (AC1GsaGTPCaMCA4, AC1GsaGTPCaMCA4ATP), (AC1GsaGTPGiaGTPCaMCA4, AC1GsGiCaMCA4ATP), (AC1GsaGTPCaMCA4, AC1GsaGTPCaMCA4ATP), (AC1CaMCA4, AC1CaMCA4ATP), (AC8CaMCA4, AC8CaMCA4ATP) \}$	$_memb_S845_S831, PKCp \}$
$(\mathbf{X}_8, \mathbf{Y}_8, \mathbf{Z}_8) \in \{ (GiaGTP, AC1GsaGTP, GTPGiaGTP), (GiaGTP, AC1CaMCA4, GTPCaMCA4), (AC1GsaGTP, GsaGTP, GTPGiaGTP) \}$	$(\mathbf{X}_{24}, \mathbf{Z}_{24}) \in \{ (_S831, _S831_PKAc), (_memb_S831, _memb_S831_PKAc) \}$
$(\mathbf{X}_9, \mathbf{Z}_9) \in \{ (AC1GsGiCaMCA4ATP, AC1GsaGTPGiaGTPCaMCA4), (AC8CaMCA4ATP, AC8CaMCA4) \}$	$(\mathbf{X}_{25}, \mathbf{Z}_{25}) \in \{ (_S845, _S845_PP1), (_memb_S845, _memb_S845_PP1) \}$
$(\mathbf{X}_{10}, \mathbf{Z}_{10}) \in \{ (CaMCA2, CaMCA3), (PP2BCaMCA2, PP2BCaMCA3) \}$	$(\mathbf{X}_{26}, \mathbf{Y}_{26}) \in \{ (_S845_PP1, \{\}), (_memb_S845_PP1, _memb_S845_PP1) \}$
$(\mathbf{X}_{11}, \mathbf{Z}_{11}) \in \{ (CaMCA3, CaMCA4), (PP2BCaMCA3, PP2BCaMCA4) \}$	$(\mathbf{X}_{27}, \mathbf{Z}_{27}) \in \{ (_S845_S831, _S845_S831_PP1), (_S831, _S831_PP1), (_memb_S845_S831, _memb_S845_S831_PP1), (_memb_S831, _memb_S831_PP1) \}$
$(\mathbf{X}_{12}, \mathbf{Z}_{12}) \in \{ (2, CaMCA2), (4, CaMCA4) \}$	$(\mathbf{X}_{28}, \mathbf{Y}_{28}) \in \{ (_S845_S831_PP1, _S845), (_S845_S831_PP1, _S831), (_S831_PP1, \{\}), (_memb_S845_S831_PP1, _memb_S845), (_memb_S845_S831_PP1, _memb_S831), (_memb_S831_PP1, _memb) \}$
$\mathbf{X}_{13} \in \{ pCaMCA4, CaMCA4 \}$	$(\mathbf{X}_{29}, \mathbf{Z}_{29}) \in \{ (_S845, _S845_PP2B), (_S845_S831, _S845_S831_PP2B), (_memb_S845, _memb_S845_PP2B), (_memb_S845_S831, _memb_S845_S831_PP2B) \}$
$(\mathbf{X}_{14}, \mathbf{Z}_{14}) \in \{ (\{\}, PP1), (CaMCA4, CaMCA4PP1) \}$	$(\mathbf{X}_{30}, \mathbf{Y}_{30}) \in \{ (_S845_PP2B, \{\}), (_S845_S831_PP2B, _S831), (_memb_S845_PP2B, _memb), (_memb_S845_S831_PP2B, _memb_S831) \}$
$(\mathbf{X}_{15}, \mathbf{Z}_{15}) \in \{ (PP1, \{\}), (CaMCA4PP1, CaMCA4) \}$	$\mathbf{X}_{31} \in \{ (\{\}, _PKAc, _CKCam, _CKpCam, _CKp, _PKCt, _PKCp, _S831, _S831_PKAc, _S831_PP1) \}$
$(\mathbf{X}_{16}, \mathbf{Z}_{16}) \in \{ (\{\}, CaMCA4), (PP1, P2BCaMCA4) \}$	$\mathbf{X}_{32} \in \{ (\{\}, _CKCam, _CKpCam, _CKp, _PKCt, _PKCp, _S831, _PP1, _S831_PP1, _PP2B, _S831_PP2B) \}$
$\mathbf{X}_{17} \in \{ CaMCA4, P2BCaMCA4 \}$	$(\mathbf{X}_{33}, \mathbf{Y}_{33}, \mathbf{Z}_{33}) \in \{ (PKAc, PDE4, PDE4), (PDE4cAMP, PKAc, _PDE4_cAMP) \}$
$(\mathbf{X}_{18}, \mathbf{Z}_{18}) \in \{ (\{\}, _PKAc), (_memb, _memb_PKAc) \}$	$(\mathbf{X}_{34}, \mathbf{Y}_{34}) \in \{ (PDE4, \{\}), (_PDE4_cAMP, cAMP) \}$
$(\mathbf{X}_{19}, \mathbf{Y}_{19}) \in \{ (_PKAc, _S845), (_S831_PKAc, _S845_S831), (_memb_PKAc, _memb_S845), (_memb_S831_PKAc, _memb_S845_S831) \}$	$(\mathbf{X}_{35}, \mathbf{Y}_{35}) \in \{ (GqaGTP, \{\}), (CaGqaGTP, Ca) \}$
$(\mathbf{X}_{20}, \mathbf{Y}_{20}, \mathbf{Z}_{20}) \in \{ (\{\}, CaMCA4, _CKCam), (\{\}, p, _CKp), (_S845, CaMCA4, _S845_CKCam), (_S845, p, _S845_CKp), (_memb, CaMCA4, _memb_CKCam), (_memb, p, _memb_CKp), (_memb_S845, CaMCA4, _memb_S845_CKCam), (_memb_S845, p, _memb_S845_CKp) \}$	$(\mathbf{X}_{36}, \mathbf{Y}_{36}, \mathbf{Z}_{36}) \in \{ (\{\}, t, _PKCt), (\{\}, p, _PKCp), (_memb, t, _memb_PKCt), (_memb, p, _memb_PKCp) \}$
$(\mathbf{X}_{21}, \mathbf{Y}_{21}, \mathbf{Z}_{21}) \in \{ (_CKCam, _S831, CaMCA4), (_CKp, _S831, p), (_S845_CKCam, _S845_S831, CaMCA4), (_S845_CKp, _S845_S831, p), (_memb_CKCam, _memb_S831, CaMCA4), (_memb_CKp, _memb_S831, p), (_memb_S845_CKCam, _memb_S845_S831, CaMCA4), (_memb_S845_CKp, _memb_S845_S831, p) \}$	$(\mathbf{X}_{37}, \mathbf{Y}_{37}, \mathbf{Z}_{37}) \in \{ (_PKCt, _S880, t), (_PKCp, _S880, p), (_memb_PKCt, _memb_S880, t), (_memb_PKCp, _memb_S880, p) \}$
$(\mathbf{X}_{22}, \mathbf{Y}_{22}, \mathbf{Z}_{22}) \in \{ (\{\}, CKpCaMCA4, _CKpCam), (\{\}, PKCt, _PKCt), (\{\}, PKCp, _PKCp), (_S845, CKpCaMCA4, _S845_CKpCam), (_S845, PKCt, _S845_PKCt), (_S845, PKCp, _S845_PKCp), (_memb, CKpCaMCA4, _memb_CKpCam), (_memb, PKCt, _memb_PKCt), (_memb, PKCp, _memb_PKCp), (_memb_S845, CKpCaMCA4, _memb_S845_CKpCam), (_memb_S845, PKCt, _memb_S845_PKCt), (_memb_S845, PKCp, _memb_S845_PKCp) \}$	$(\mathbf{X}_{38}, \mathbf{Z}_{38}) \in \{ (_S880, _S880_PP2A), (_memb_S880, _memb_S880_PP2A) \}$
$(\mathbf{X}_{23}, \mathbf{Y}_{23}, \mathbf{Z}_{23}) \in \{ (_S845, CKpCaMCA4, _S845_CKpCam), (_S845, PKCt, _S845_PKCt), (_S845, PKCp, _S845_PKCp), (_memb, CKpCaMCA4, _memb_CKpCam), (_memb, PKCt, _memb_PKCt), (_memb, PKCp, _memb_PKCp), (_memb_S845, CKpCaMCA4, _memb_S845_CKpCam), (_memb_S845, PKCt, _memb_S845_PKCt), (_memb_S845, PKCp, _memb_S845_PKCp) \}$	$\mathbf{X}_{39} \in \{ (_S880_PP2A, \{\}), (_memb_S880_PP2A, _memb) \}$
$(\mathbf{X}_{24}, \mathbf{Z}_{24}) \in \{ (_S831, _S831_PKAc), (_memb_S831, _memb_S831_PKAc) \}$	$\mathbf{X}_{40} \in \{ (\{\}, _PKCt, _PKCp) \}$
$(\mathbf{X}_{25}, \mathbf{Z}_{25}) \in \{ (_S845, _S845_PP1), (_memb_S845, _memb_S845_PP1) \}$	$\mathbf{X}_{41} \in \{ (\{\}, _PP2A) \}$

Table 4. List of initial concentrations of molecular species.

All non-mentioned species have an initial concentration of 0 nM.

Species	Conc. (nM)	Species	Conc. (nM)	Species	Conc. (nM)
CaOut extracell. Ca ²⁺	1900000	AMP adenosine monophosphate	980	Pip2 phosphatidylinositol 4,5-bisphosphate	24000
Leak leak channels	2000	Ng neurogranin	20000	Plkinase phosphatidylinositol kinase	290
Calbin calbindin	150000	CaM calmodulin	60000	Ip3degPlk Ip3-bound PI kinase	400
CalbinC Ca ²⁺ -bound calbindin	15000	PP2B protein phosphatase 2B	2300	PKC protein kinase C	15000
LOut extracell. β-adr. ligand	2500000	CK CaMKII	23000	DAG diacylglycerol	90
Epac1 Epac1	500	PKA protein kinase A	6400	DAGK DAG kinase	300
PMCA Ca ²⁺ pump	22000	I1 inhibitor-1	2200	DGL DAG lipase	1600
NCX Ca ²⁺ exchanger	540000	PP1 protein phosphatase 1	1600	CaDGL Ca ²⁺ -bound DAG lipase	250
L β-adrenergic ligand	10	GluR1 AMPAR subunit type 1	180	DAGCaDGL Ca ²⁺ -and DAG-bound DAG lipase	90
R β-adrenergic receptor	1600	GluR1_memb membrane-inserted GluR1	90	Ip3degrad degraded Ip3	600
Gs S-type G-protein	13000	PDE4 phosphodiesterase type 4	670	GluR2 AMPAR subunit type 2	14
Gi I-type G-protein	2600	fixedbuffer immobile buffer	500000	GluR2_memb membrane-inserted GluR2	256
AC1 adenylyl cyclase type 1	430.0	mGluR metab. glutamate receptor	800	PP2A protein phosphatase 2A	500
ATP adenosine triphosphate	2000000	GluOut extracell. glutamate	1000000	M1R acetylcholine receptor M1	450
AC8 adenylyl cyclase type 8	370	Gqabg Q-type G-protein	1400	PLA2 phospholipase A2	1000
PDE1 phosphodiesterase type 1	12000	PLC phospholipase C	250		

Materials and methods

Construction and calibration of the biochemically detailed model of post-synaptic plasticity in the cortex

We created a model of pathways leading from Ca²⁺ inputs and activation of β-adrenergic receptors, metabotropic glutamate receptors, and muscarinic acetylcholine receptors to the phosphorylation and insertion of AMPARs into the membrane. We started by using the model of *Jędrzejewska-Szmek et al., 2017* for GluR1 phosphorylation at sites S831 and S845, which are phosphorylated by PKA and CaMKII, respectively, as a basis for our unified model. We added the mGluR- and M1 receptor-dependent pathways leading to PKC activation from *Kim et al., 2013* and *Blackwell et al., 2019*, respectively, and adopted the PKC-dependent endocytosis of GluR2 and reinsertion to the membrane from *Gallimore et al., 2018* as these pathways are critical for neocortical plasticity (*Seol et al., 2007*). As we included molecular species from different models and as we omitted certain molecular species that affected the dynamics of the underlying species but were not imperative for the pathways we wanted to describe, calibration of the model reactions was necessary. Following *Hayer and Bhalla, 2005*, we allowed the insertion and removal of GluR1 subunits to and from the membrane that depended on their state of S845 phosphorylation. We also allowed spontaneous membrane insertion of non-S845-phosphorylated GluR1; we chose the rate of this reaction so that on average one fifth of the (non-S845-phosphorylated) GluR1s were membrane-expressed in steady state, as suggested by experimental data (*Oh et al., 2006*). We adjusted the forward rate of GluR2 insertion to the membrane to decrease the proportion of membrane-inserted vs. internalised GluR2s (**Figure 11A**), following experimental data according to which 45% of GluR2s were membrane-

inserted at resting conditions (Ashby et al., 2004). We also adopted the three-step CaM activation of Gallimore et al., 2018 instead of the two-step activation of Jędrzejewska-Szmek et al., 2017 where the reaction rates of CaM binding two Ca^{2+} ions were linearly dependent on the number of Ca^{2+} ions. The response curve for CaM activation by Ca^{2+} was steeper in this model (Figure 11B), which was in better accordance with recent experimental data (Hoffman et al., 2014). As a result, our model predicted a more prominent activation of CaM in response to a large influx of Ca^{2+} but milder activation in response to small Ca^{2+} influx than the model of Jędrzejewska-Szmek et al., 2017 (Figure 11C).

To allow long-term activation of PKC, we adopted a persistently activated form of PKC, mediated by arachidonic acid (AA), from Koteleski et al., 2002. We calibrated the rates of this reaction as follows. The backward rate was chosen so that approximately 90% of PKC would be active after 10 min, inspired by experimental data of Shirai et al., 1998. The forward rate was chosen so that LFS with effective PLC activation led to approximately 50% of the GluR2s being phosphorylated (Figure 11D), following experimental data (Ahmadian et al., 2004). The implications of these adjustments on the dynamics of transiently activated PKC, persistently activated PKC and GluR2 S880 phosphorylation are illustrated in Figures 11E, F and G, respectively.

We adopted the simplified, mass-action law-based PKA activation model (reaction 59; Table 3) from Williamson et al., 2009 (where it was called model 'C') instead of the 2-stage, linearised cAMP-binding of PKA in Jędrzejewska-Szmek et al., 2017 and Blackwell et al., 2019. We fitted the forward rate to data simulated with the original model (Figure 11H) to produce a longer-lasting S845 phosphorylation (typically, >10 min duration of S845 phosphorylation was observed Seol et al., 2007; Xue et al., 2014) in the 4xHFS protocol (Figure 11I). To account for the experimental observation the PKC phosphorylates GluR1 at site S831 Roche et al., 1996, we added this reaction using the rates identical to those of GluR1-S831 phosphorylation by phosphorylated CaMKII (see reactions 71–72). However, the presence of this reaction did not have a large effect on the S831 phosphorylation of GluR1 under standard conditions (Figure 11J). Finally, we introduced an immobile Ca^{2+} buffer with a Ca^{2+} binding rate of 0.0004 1/(nM ms), a release rate 20.0 1/ms, and an initial concentration of 500 μM (these values are within the range of experimental observations and values used in models Matthews and Dietrich, 2015). The model reactions are described in Table 3 and the initial concentrations are listed in Table 4.

Throughout the work, we simulated the signalling pathways in a single compartment representing a dendritic spine of size 0.5 μm^3 . In reality, some of the molecular species are prevalently present in the cytosol, some attached to the membrane, some in the extracellular medium in an immediate vicinity to the membrane, and others outside the cell further away from the synaptic cleft (free in the extracellular medium or sequestered to other cells). As commonly done in the field, we solved this problem by introducing species that represent a molecular species confined in a particular location: reactions 1–6 describe the extrusion of Ca^{2+} from the cytosol into the extracellular medium, reactions 8, 95, and 135 describe the escape of ligands from the vicinity of the synapse, and reactions 80–81 and 128–129 for the translocation of the AMPARs to/from the membrane (Table 3). All stimulations start after 4040 s of simulation without inputs, which is sufficient for attaining a steady state for all species (Figure 11—figure supplement 1).

Statistical model for numbers of AMPAR tetramers at the membrane and the total synaptic conductance

AMPARs have different conductances depending on their subunit composition and phosphorylation state (Oh and Derkach, 2005), but it is challenging to take this into account in models that include a large number of receptor subunits. In our model, AMPAR subunits GluR1 and GluR2 can be in one of 21 or five states, respectively, when counting all the different phosphorylation states and bonds with other molecules (Table 3), which leads to 28^4 possible types of tetramers. This makes it virtually impossible to model the dynamics of AMPAR tetramer assembly using the mass-action law-based approach where the concentration of each type of species is monitored (Michalski and Loew, 2012). To avoid this problem, we used a statistical model that estimated the numbers and types of different types of AMPAR tetramers given the numbers of GluR1 and GluR2 subunits located at the membrane.

We assumed that the composition of AMPAR tetramers is random such that there is no preference of one type of subunit being more likely to bind with any other type of subunit. Thus, the

probability of a tetramer being a GluR1 homomer without any S831-phosphorylated subunits is approximately

$$p_{\text{GluR1 homomer, non-phos.}} = \frac{\binom{N_1 - N_{1,\text{phos.}}}{4}}{\binom{N_1 + N_2}{4}} \approx \frac{(N_1 - N_{1,\text{phos.}})^4}{(N_1 + N_2)^4} \quad (1)$$

where N_1 and N_2 are the numbers of GluR1 and GluR2 subunits bound to the membrane, respectively, and $N_{1,\text{phos.}}$ is the number of S831-phosphorylated GluR1 subunits at the membrane (note that the $N_{1,\text{phos.}}$ subunits are included in all GluR1 subunits, that is, $N_{1,\text{phos.}} \leq N_1$). Accordingly, the probabilities of a tetramer being a GluR1 homomer with at least one S831-phosphorylated subunit, a GluR2 homomer, or a heteromer, are approximately:

$$r p_{\text{GluR1 homomer, phos.}} = \frac{N_1^4 - (N_1 - N_{1,\text{phos.}})^4}{(N_1 + N_2)^4} \quad (2)$$

$$p_{\text{GluR2 homomer}} = \frac{N_2^4}{(N_1 + N_2)^4} \quad (3)$$

$$p_{\text{heteromer}} = 1 - \frac{N_1^4}{(N_1 + N_2)^4} - \frac{N_2^4}{(N_1 + N_2)^4}. \quad (4)$$

The number of membrane-bound tetramers that the N_1 GluR1 subunits and N_2 GluR2 subunits at the membrane can form is $\frac{N_1 + N_2}{4}$. Here, we ignore the unpaired subunits by estimating that $\frac{N_1 + N_2}{4} \approx \lfloor \frac{N_1 + N_2}{4} \rfloor$ — we also disregard the states of the non-membrane-bound subunits as they are not assumed to contribute to the synaptic conductance. This gives us approximate values for expected numbers of different types of tetramers on the membrane:

$$\begin{aligned} N_{\text{GluR1 homomer, non-phos.}} &= \frac{N_1 + N_2}{4} p_{\text{GluR1 homomer, non-phos.}} \\ N_{\text{GluR1 homomer, phos.}} &= \frac{N_1 + N_2}{4} r p_{\text{GluR1 homomer, phos.}} \\ N_{\text{GluR2 homomer}} &= \frac{N_1 + N_2}{4} p_{\text{GluR2 homomer}} \\ N_{\text{heteromer}} &= \frac{N_1 + N_2}{4} p_{\text{heteromer}} \end{aligned}$$

These estimates allow us to determine the total maximal synaptic conductance as the sum of the numbers of these tetramers multiplied with the corresponding single-channel conductances:

$$g_{\text{syn}} = 12.4\text{pS} \times N_{\text{GluR1 homomer, non-phos.}} + 18.9\text{pS} \times N_{\text{GluR1 homomer, phos.}} + 2.2\text{pS} \times N_{\text{GluR2 homomer}} + 2.5\text{pS} \times N_{\text{heteromer}}. \quad (5)$$

The single-channel conductance values 12.4 pS, 18.9 pS, 2.2 pS, and 2.5 pS are taken from experimental data (Oh and Derkach, 2005).

Modelling the Ca²⁺ inputs and neuromodulatory inputs

We modelled the neurotransmission to the post-synaptic spine as fluxes of Ca²⁺ ions, β-adrenergic ligand, glutamate, and acetylcholine (labelled as Ca, L, Glu, and ACh, respectively, in Table 3). We used various stimulation paradigms: In sections ‘Ca²⁺ activates multiple pathways that regulate the post-synaptic plasticity in cortical PCs’ and ‘The model predicts multimodal, protein concentration- and neuromodulation-dependent rules of plasticity’, long-lasting, single pulses of input species were applied. In sections ‘High-frequency stimulation (HFS) causes LTP and low-frequency stimulation (LFS) causes LTD in GluR1-GluR2-balanced synapses’ and ‘A parametric analysis confirms the robustness of the model’, we used the following repeated stimulus protocols: HFS — 100 pulses of Ca²⁺ (3 ms), repeated at 100 Hz; 4xHFS — 4 trains of HFS, separated by 3 s of quiescence; LFS — 900 pulses of Ca²⁺ (3 ms), repeated at 5 Hz. Unless otherwise stated, each Ca²⁺ pulse was accompanied by a 3 ms pulse of β-adrenergic ligand, glutamate, and acetylcholine. The activation of cholinergic and noradrenergic terminals by electrical stimulation is supported by experimental data in, e.g., slices of mouse prefrontal cortex (Mundorf et al., 2001). In section ‘The model flexibly reproduces data from

various cortical LTP/LTD experiments', the same approach was used, but the frequencies and numbers of repetitions of the inputs were taken from the experiments (see [Table 2](#)).

In section 'Paired pre- and post-synaptic stimulation induces PKA- and PKC-dependent spike-timing-dependent plasticity (STDP) in GluR1-GluR2-balanced synapses' (and [Figure 3—figure supplement 3](#) of section 'High-frequency stimulation (HFS) causes LTP and low-frequency stimulation (LFS) causes LTD in GluR1-GluR2-balanced synapses'), we used a multicompartmental model of a layer 2/3 pyramidal cell ([Markram et al., 2015](#)) (L23_PC_cADpyr229_1) to determine the amplitudes and time courses of the Ca^{2+} inputs conducted by NMDARs when different stimulus patterns were applied. This model included the fast Na^+ current $I_{\text{Na,t}}$, Shaw-related K^+ current $I_{\text{Kv3.1}}$, muscarinic K^+ current I_{m} , and hyperpolarization-activated cyclic nucleotide-gated current I_{HCN} in the apical dendrite. The axo-somatic region contained all these (except for I_{m}) as well as the low and high-voltage activated Ca^{2+} currents I_{CaLVA} and I_{CaHVA} , the small-conductance Ca^{2+} -dependent K^+ current I_{SK} , the transient K^+ current $I_{\text{K,t}}$, and the persistent Na^+ and K^+ currents $I_{\text{Na,p}}$ and $I_{\text{K,p}}$ in the axo-somatic region ([Markram et al., 2015](#)). We placed 10 post-synaptic spines, consisting of a 0.5 μm long and 0.1 μm thick neck and a 0.4 μm long and 0.4 μm thick head, to the proximal apical dendrite (250–300 μm from the soma). For an analysis of the effects of synapse location on Ca^{2+} flux and plasticity in cortical pyramidal cells, see [Ebner et al., 2019](#). Each spine was equipped with the AMPA–NMDA synapse model of [Hay and Segev, 2015](#) using the NMDA gating mechanism of [Spruston et al., 1995](#) and an adjustment in the pre-synaptic resource update ([Mäki-Marttunen et al., 2019](#)). The ten synapses were synchronously stimulated but the glutamate release was probabilistic, the release events at different synapses being independent of each other as in [Hay and Segev, 2015](#)). We set the maximal AMPAR conductance to 0.001 μS , a value typically used in computational neuron models. We set the maximal conductance of NMDARs to 0.0032 μS to compensate for the lack of the slow component in the model of the NMDA current ([Markram et al., 2015](#)) — a value significantly smaller or larger than this abolished the LTP or LTD, respectively, in our STDP model, while the AMPAR conductance was a less crucial parameter ([Figure 11—figure supplement 2](#)). We estimated the numbers of Ca^{2+} ions entering into the post-synaptic spine across time, and used these numbers as the input to the biochemical model. In section 'Paired pre- and post-synaptic stimulation induces PKA- and PKC-dependent spike-timing-dependent plasticity (STDP) in GluR1-GluR2-balanced synapses', following the experiments of [Seol et al., 2007](#), we used extracellular $[\text{Mg}^{2+}]$ of 1.0 mM and a 1 Hz pre-synaptic stimulation, where each pulse was paired with a burst of post-synaptic stimulus currents ([Seol et al., 2007](#)). For [Figure 3—figure supplement 3](#) of section 'High-frequency stimulation (HFS) causes LTP and low-frequency stimulation (LFS) causes LTD in GluR1-GluR2-balanced synapses', following the experiments of [Heusler et al., 2000](#) we used $[\text{Mg}^{2+}]$ of 1.3 mM and solely pre-synaptic stimulation of one of the two stimulus protocols: 6xHFSt — 10 bursts of 4 pulses (at 100 Hz), repeated every 100 ms, and the whole train repeated 6 times every 10 s; LFS-1Hz — 1800 pulses delivered at a frequency of 1 Hz.

The effects of LTP/LTD on the size of Ca^{2+} inputs were not considered in this work.

Parameter alterations and model fitting

In sections 'The model predicts multimodal, protein concentration- and neuromodulation-dependent rules of plasticity' and 'The model flexibly reproduces data from various cortical LTP/LTD experiments', we altered the initial concentrations of many proteins to explore the parameter space or to perform model fitting. We chose to fit protein concentrations instead of reaction rates, since the reaction rates can be considered to be the same across cell types while the protein expression is known to be cell-type and age-dependent. This is analogous to fitting maximal conductances that correlate with ion-channel densities in Hodgkin-Huxley-type models instead of the ion-channel activation and inactivation curve parameters as is usually done in the fitting of biophysically detailed neuron models. The concentrations of upstream PKA-pathway proteins R (β -adrenergic receptor), Gs, AC1, and AC8 were varied in proportion using a factor parameter $f_{\text{PKA}} \in [0, 2]$, and, likewise, the concentrations of upstream PKC-pathway proteins mGluR, M1, Gq, and PLC using a factor parameter $f_{\text{PKC}} \in [0, 2]$. Furthermore, in section 'The model flexibly reproduces data from various cortical LTP/LTD experiments', CaM and CaMKII were altered in proportion by a factor $f_{\text{CaMKII}} \in [0, 2]$, phosphatases PP1 and PP2B by a factor $f_{\text{PP}} \in [0, 2]$, and phosphodiesterases PDE1 and PDE4 by a factor $f_{\text{PDE}} \in [0, 2]$. In both sections, the rapidity of Ca^{2+} extrusion was varied by altering the concentration of NCX, and in section 'The model flexibly reproduces data from various cortical LTP/LTD

experiments', the concentrations of PKA and PKC were varied in addition to the upstream proteins — these concentrations were varied within the interval from 0 to double the original value. For the multi-objective optimisation in section 'The model flexibly reproduces data from various cortical LTP/LTD experiments', we used the Python implementation (published by the authors of *Bahl et al., 2012*) of the non-dominated sorting genetic algorithm II (NSGA-II) (*Deb et al., 2002*) with population size 1000. To restrict to physiologically realistic Ca^{2+} dynamics, we disregarded the data where free Ca^{2+} concentrations rose above 2 μM for one or more levels of Ca^{2+} input in section 'The model predicts multimodal, protein concentration- and neuromodulation-dependent rules of plasticity'. In a similar manner, in section 'The model flexibly reproduces data from various cortical LTP/LTD experiments', we introduced an objective function that penalised parameter sets that produced Ca^{2+} transients larger than 2 μM .

Simulation software and code accessibility

For deterministic simulations of intracellular signalling, we used the NEURON simulator with the reaction-diffusion (RxD) extension (*McDougal et al., 2013*). For stochastic simulations, we used NeuroRD software (<https://github.com/neuroRD>). In both types of simulations, we used adaptive time-step integration methods. The NEURON simulator was also used for simulating the multicompartmental model of layer 2/3 pyramidal cell in section 'Paired pre- and post-synaptic stimulation induces PKA- and PKC-dependent spike-timing-dependent plasticity (STDP) in GluR1-GluR2-balanced synapses'. The full model along with the fitting and data-analysis algorithms (Python scripts) that were used in this study are publicly available in ModelDB at <http://modeldb.yale.edu/260971>.

Acknowledgements

UNINETT Sigma2 resources (project NN9529K) were used for simulations. Funding: Research Council of Norway (248828), European Union Horizon 2020 Research and Innovation Programme under Grant Agreement No. 785907 [Human Brain Project (HBP) SGA2].

Additional information

Funding

Funder	Grant reference number	Author
Research Council of Norway	248828	Tuomo Mäki-Marttunen Andrew G Edwards Gaute T Einevoll
Horizon 2020 - Research and Innovation Framework Programme	785907	Gaute T Einevoll

The funders had no role in study design, data collection and interpretation, or the decision to submit the work for publication.

Author contributions

Tuomo Mäki-Marttunen, Conceptualization, Software, Validation, Investigation, Methodology, Writing - original draft, Project administration, Writing - review and editing; Nicolangelo Iannella, Andrew G Edwards, Gaute T Einevoll, Formal analysis, Methodology; Kim T Blackwell, Conceptualization, Software, Supervision, Methodology

Author ORCIDs

Tuomo Mäki-Marttunen  <https://orcid.org/0000-0002-7082-2507>

Gaute T Einevoll  <http://orcid.org/0000-0002-5425-5012>

Kim T Blackwell  <http://orcid.org/0000-0003-4711-2344>

Decision letter and Author response

Decision letter <https://doi.org/10.7554/eLife.55714.sa1>

Author response <https://doi.org/10.7554/eLife.55714.sa2>

Additional files

Data availability

All data generated or analysed during this study are included in the manuscript and supporting files. Simulation scripts can be found at <http://modeldb.yale.edu/260971>.

The following dataset was generated:

Author(s)	Year	Dataset title	Dataset URL	Database and Identifier
Mäki-Marttunen T, Iannella N, Edwards AG, Einevoll GT, Blackwell KT	2020	Biochemically detailed model of LTP and LTD in a cortical spine (Maki-Marttunen et al 2020)	http://modeldb.yale.edu/260971	ModelDB, 260971

References

- Ahmadian G, Ju W, Liu L, Wyszynski M, Lee SH, Dunah AW, Taghibiglou C, Wang Y, Lu J, Wong TP, Sheng M, Wang YT. 2004. Tyrosine phosphorylation of GluR2 is required for insulin-stimulated AMPA receptor endocytosis and LTD. *The EMBO Journal* **23**:1040–1050. DOI: <https://doi.org/10.1038/sj.emboj.7600126>, PMID: 14976558
- Ashby MC, De La Rue SA, Ralph GS, Uney J, Collingridge GL, Henley JM. 2004. Removal of AMPA receptors from synapses is preceded by transient endocytosis of extrasynaptic AMPARs. *Journal of Neuroscience* **24**:5172–5176. DOI: <https://doi.org/10.1523/JNEUROSCI.1042-04.2004>, PMID: 15175386
- Badoual M, Zou Q, Davison AP, Rudolph M, Bal T, Frégnac Y, Destexhe A. 2006. Biophysical and phenomenological models of multiple spike interactions in spike-timing dependent plasticity. *International Journal of Neural Systems* **16**:79–97. DOI: <https://doi.org/10.1142/S0129065706000524>, PMID: 16688849
- Bahl A, Stemmler MB, Herz AV, Roth A. 2012. Automated optimization of a reduced layer 5 pyramidal cell model based on experimental data. *Journal of Neuroscience Methods* **210**:22–34. DOI: <https://doi.org/10.1016/j.jneumeth.2012.04.006>, PMID: 22524993
- Banerjee B, Medda BK, Pochiraju S, Kannampalli P, Lang IM, Sengupta JN, Shaker R. 2013. AMPA receptor subunits expression and phosphorylation in cingulate cortex in rats following esophageal acid exposure. *Neurogastroenterology & Motility* **25**:973–e776. DOI: <https://doi.org/10.1111/nmo.12233>, PMID: 24118589
- Bear MF, Cooper LN, Ebner FF. 1987. A physiological basis for a theory of synapse modification. *Science* **237**:42–48. DOI: <https://doi.org/10.1126/science.3037696>, PMID: 3037696
- Bhalla US, Iyengar R. 1999. Emergent properties of networks of biological signaling pathways. *Science* **283**:381–387. DOI: <https://doi.org/10.1126/science.283.5400.381>, PMID: 9888852
- Bi GQ, Poo MM. 1998. Synaptic modifications in cultured hippocampal neurons: dependence on spike timing, synaptic strength, and postsynaptic cell type. *The Journal of Neuroscience* **18**:10464–10472. DOI: <https://doi.org/10.1523/JNEUROSCI.18-24-10464.1998>, PMID: 9852584
- Bienenstock EL, Cooper LN, Munro PW. 1982. Theory for the development of neuron selectivity: orientation specificity and binocular interaction in visual cortex. *The Journal of Neuroscience* **2**:32–48. DOI: <https://doi.org/10.1523/JNEUROSCI.02-01-00032.1982>, PMID: 7054394
- Blackwell KT, Salinas AG, Tewatia P, English B, Hellgren Kotaleski J, Lovinger DM. 2019. Molecular mechanisms underlying striatal synaptic plasticity: relevance to chronic alcohol consumption and seeking. *European Journal of Neuroscience* **49**:768–783. DOI: <https://doi.org/10.1111/ejn.13919>, PMID: 29602186
- Brzosko Z, Mierau SB, Paulsen O. 2019. Neuromodulation of Spike-Timing-Dependent plasticity: past, present, and future. *Neuron* **103**:563–581. DOI: <https://doi.org/10.1016/j.neuron.2019.05.041>, PMID: 31437453
- Cai X, Gu Z, Zhong P, Ren Y, Yan Z. 2002. Serotonin 5-HT1A receptors regulate AMPA receptor channels through inhibiting Ca²⁺/calmodulin-dependent kinase II in prefrontal cortical pyramidal neurons. *The Journal of Biological Chemistry* **277**:36553–36562. DOI: <https://doi.org/10.1074/jbc.M203752200>, PMID: 12149253
- Castellani GC, Quinlan EM, Cooper LN, Shouval HZ. 2001. A biophysical model of bidirectional synaptic plasticity: dependence on AMPA and NMDA receptors. *PNAS* **98**:12772–12777. DOI: <https://doi.org/10.1073/pnas.201404598>, PMID: 11675507
- Castellani GC, Quinlan EM, Bersani F, Cooper LN, Shouval HZ. 2005. A model of bidirectional synaptic plasticity: from signaling network to channel conductance. *Learning & Memory* **12**:423–432. DOI: <https://doi.org/10.1101/lm.80705>, PMID: 16027175
- Castro-Alamancos MA, Donoghue JP, Connors BW. 1995. Different forms of synaptic plasticity in somatosensory and motor Areas of the neocortex. *The Journal of Neuroscience* **15**:5324–5333. DOI: <https://doi.org/10.1523/JNEUROSCI.15-07-05324.1995>, PMID: 7623155

- Chung HJ**, Xia J, Scannevin RH, Zhang X, Hugarir RL. 2000. Phosphorylation of the AMPA receptor subunit GluR2 differentially regulates its interaction with PDZ domain-containing proteins. *The Journal of Neuroscience* **20**:7258–7267. DOI: <https://doi.org/10.1523/JNEUROSCI.20-19-07258.2000>, PMID: 11007883
- Cornelisse LN**, van Elburg RA, Meredith RM, Yuste R, Mansvelter HD. 2007. High speed two-photon imaging of calcium dynamics in dendritic spines: consequences for spine calcium kinetics and buffer capacity. *PLOS ONE* **2**:e1073. DOI: <https://doi.org/10.1371/journal.pone.0001073>, PMID: 17957255
- D'Alcantara P**, Schiffmann SN, Swillens S. 2003. Bidirectional synaptic plasticity as a consequence of interdependent Ca²⁺-controlled phosphorylation and dephosphorylation pathways. *European Journal of Neuroscience* **17**:2521–2528. DOI: <https://doi.org/10.1046/j.1460-9568.2003.02693.x>, PMID: 12823459
- Deb K**, Pratap A, Agarwal S, Meyarivan T. 2002. A fast and elitist multiobjective genetic algorithm: nsga-ii. *IEEE Transactions on Evolutionary Computation* **6**:182–197. DOI: <https://doi.org/10.1109/4235.996017>
- Devor A**, Andreassen OA, Wang Y, Mäki-Marttunen T, Smeland OB, Fan CC, Schork AJ, Holland D, Thompson WK, Witoelar A, Chen CH, Desikan RS, McEvoy LK, Djurovic S, Greengard P, Svenningsson P, Einevoll GT, Dale AM. 2017. Genetic evidence for role of integration of fast and slow neurotransmission in schizophrenia. *Molecular Psychiatry* **22**:792–801. DOI: <https://doi.org/10.1038/mp.2017.33>, PMID: 28348379
- Di Cristo G**, Berardi N, Cancedda L, Pizzorusso T, Putignano E, Ratto GM, Maffei L. 2001. Requirement of ERK activation for visual cortical plasticity. *Science* **292**:2337–2340. DOI: <https://doi.org/10.1126/science.1059075>, PMID: 11423664
- Diering GH**, Heo S, Hussain NK, Liu B, Hugarir RL. 2016. Extensive phosphorylation of AMPA receptors in neurons. *PNAS* **113**:E4920–E4927. DOI: <https://doi.org/10.1073/pnas.1610631113>, PMID: 27482106
- Ebner C**, Clopath C, Jedlicka P, Cuntz H. 2019. Unifying Long-Term plasticity rules for excitatory synapses by modeling dendrites of cortical pyramidal neurons. *Cell Reports* **29**:4295–4307. DOI: <https://doi.org/10.1016/j.celrep.2019.11.068>, PMID: 31875541
- Evans RC**, Blackwell KT. 2015. Calcium: amplitude, duration, or location? *The Biological Bulletin* **228**:75–83. DOI: <https://doi.org/10.1086/BBLv228n1p75>, PMID: 25745102
- Feldman DE**. 2009. Synaptic mechanisms for plasticity in neocortex. *Annual Review of Neuroscience* **32**:33–55. DOI: <https://doi.org/10.1146/annurev.neuro.051508.135516>, PMID: 19400721
- Flores O**, Pérez H, Valladares L, Morgan C, Gatica A, Burgos H, Olivares R, Hernández A. 2011. Hidden prenatal malnutrition in the rat: role of β_1 -adrenoceptors on synaptic plasticity in the frontal cortex. *Journal of Neurochemistry* **119**:314–323. DOI: <https://doi.org/10.1111/j.1471-4159.2011.07429.x>, PMID: 21848869
- Froc DJ**, Racine RJ. 2005. Interactions between LTP- and LTD-inducing stimulation in the sensorimotor cortex of the awake freely moving rat. *Journal of Neurophysiology* **93**:548–556. DOI: <https://doi.org/10.1152/jn.00253.2004>, PMID: 15356176
- Gallimore AR**, Kim T, Tanaka-Yamamoto K, De Schutter E. 2018. Switching on depression and potentiation in the cerebellum. *Cell Reports* **22**:722–733. DOI: <https://doi.org/10.1016/j.celrep.2017.12.084>, PMID: 29346769
- Gan Q**, Salussolia CL, Wollmuth LP. 2015. Assembly of AMPA receptors: mechanisms and regulation. *The Journal of Physiology* **593**:39–48. DOI: <https://doi.org/10.1113/jphysiol.2014.273755>, PMID: 25556786
- Granger AJ**, Nicoll RA. 2014. Expression mechanisms underlying long-term potentiation: a postsynaptic view, 10 years on. *Philosophical Transactions of the Royal Society B: Biological Sciences* **369**:20130136. DOI: <https://doi.org/10.1098/rstb.2013.0136>, PMID: 24298139
- Hardingham N**, Glazewski S, Pakhotin P, Mizuno K, Chapman PF, Giese KP, Fox K. 2003. Neocortical long-term potentiation and experience-dependent synaptic plasticity require alpha-calcium/calmodulin-dependent protein kinase II autophosphorylation. *The Journal of Neuroscience* **23**:4428–4436. DOI: <https://doi.org/10.1523/JNEUROSCI.23-11-04428.2003>, PMID: 12805283
- Hay E**, Segev I. 2015. Dendritic excitability and gain control in recurrent cortical microcircuits. *Cerebral Cortex* **25**:3561–3571. DOI: <https://doi.org/10.1093/cercor/bhu200>, PMID: 25205662
- Hayer A**, Bhalla US. 2005. Molecular switches at the synapse emerge from receptor and kinase traffic. *PLOS Computational Biology* **1**:e20. DOI: <https://doi.org/10.1371/journal.pcbi.0010020>
- He K**, Huertas M, Hong SZ, Tie X, Hell JW, Shouval H, Kirkwood A. 2015. Distinct eligibility traces for LTP and LTD in cortical synapses. *Neuron* **88**:528–538. DOI: <https://doi.org/10.1016/j.neuron.2015.09.037>, PMID: 26593091
- Heusler P**, Cebulla B, Boehmer G, Dinse HR. 2000. A repetitive intracortical microstimulation pattern induces long-lasting synaptic depression in brain slices of the rat primary somatosensory cortex. *Experimental Brain Research* **135**:300–310. DOI: <https://doi.org/10.1007/s002210000530>, PMID: 11146808
- Heynen AJ**, Yoon BJ, Liu CH, Chung HJ, Hugarir RL, Bear MF. 2003. Molecular mechanism for loss of visual cortical responsiveness following brief monocular deprivation. *Nature Neuroscience* **6**:854–862. DOI: <https://doi.org/10.1038/nn1100>, PMID: 12886226
- Hoffman L**, Chandrasekar A, Wang X, Putkey JA, Waxham MN. 2014. Neurogranin alters the structure and calcium binding properties of calmodulin. *Journal of Biological Chemistry* **289**:14644–14655. DOI: <https://doi.org/10.1074/jbc.M114.560656>, PMID: 24713697
- Holthoff K**, Tsay D, Yuste R. 2002. Calcium dynamics of spines depend on their dendritic location. *Neuron* **33**:425–437. DOI: [https://doi.org/10.1016/S0896-6273\(02\)00576-7](https://doi.org/10.1016/S0896-6273(02)00576-7), PMID: 11832229
- Honda M**, Urakubo H, Koumura T, Kuroda S. 2013. A common framework of signal processing in the induction of cerebellar LTD and cortical STDP. *Neural Networks* **43**:114–124. DOI: <https://doi.org/10.1016/j.neunet.2013.01.018>, PMID: 23500505

- Jędrzejewska-Szmek J, Luczak V, Abel T, Blackwell KT. 2017. β -adrenergic signaling broadly contributes to LTP induction. *PLOS Computational Biology* **13**:e1005657. DOI: <https://doi.org/10.1371/journal.pcbi.1005657>, PMID: 28742159
- Kantrowitz JT, Nolan KA, Epstein ML, Lehrfeld N, Shope C, Petkova E, Javitt DC. 2017. Neurophysiological effects of bitopertin in schizophrenia. *Journal of Clinical Psychopharmacology* **37**:447–451. DOI: <https://doi.org/10.1097/JCP.0000000000000722>, PMID: 28590364
- Karmarkar UR, Najarian MT, Buonomano DV. 2002. Mechanisms and significance of spike-timing dependent plasticity. *Biological Cybernetics* **87**:373–382. DOI: <https://doi.org/10.1007/s00422-002-0351-0>, PMID: 12461627
- Kim B, Hawes SL, Gillani F, Wallace LJ, Blackwell KT. 2013. Signaling pathways involved in striatal synaptic plasticity are sensitive to temporal pattern and exhibit spatial specificity. *PLOS Computational Biology* **9**:e1002953. DOI: <https://doi.org/10.1371/journal.pcbi.1002953>, PMID: 23516346
- Kirkwood A, Silva A, Bear MF. 1997. Age-dependent decrease of synaptic plasticity in the neocortex of alphaCaMKII mutant mice. *PNAS* **94**:3380–3383. DOI: <https://doi.org/10.1073/pnas.94.7.3380>, PMID: 9096402
- Kirsch L, Chechik G. 2016. On expression patterns and developmental origin of human brain regions. *PLOS Computational Biology* **12**:e1005064. DOI: <https://doi.org/10.1371/journal.pcbi.1005064>, PMID: 27564987
- Klampfl S, Maass W. 2013. Emergence of dynamic memory traces in cortical microcircuit models through STDP. *Journal of Neuroscience* **33**:11515–11529. DOI: <https://doi.org/10.1523/JNEUROSCI.5044-12.2013>, PMID: 23843522
- Koch G, Di Lorenzo F, Bonni S, Giacobbe V, Bozzali M, Caltagirone C, Martorana A. 2014. Dopaminergic modulation of cortical plasticity in Alzheimer's disease patients. *Neuropsychopharmacology* **39**:2654–2661. DOI: <https://doi.org/10.1038/npp.2014.119>, PMID: 24859851
- Komatsu Y, Toyama K, Maeda J, Sakaguchi H. 1981. Long-term potentiation investigated in a slice preparation of striate cortex of young kittens. *Neuroscience Letters* **26**:269–274. DOI: [https://doi.org/10.1016/0304-3940\(81\)90144-0](https://doi.org/10.1016/0304-3940(81)90144-0), PMID: 6275316
- Kondo M, Sumino R, Okado H. 1997. Combinations of AMPA receptor subunit expression in individual cortical neurons correlate with expression of specific calcium-binding proteins. *The Journal of Neuroscience* **17**:1570–1581. DOI: <https://doi.org/10.1523/JNEUROSCI.17-05-01570.1997>, PMID: 9030617
- Kotak VC, Breithaupt AD, Sanes DH. 2007. Developmental hearing loss eliminates long-term potentiation in the auditory cortex. *PNAS* **104**:3550–3555. DOI: <https://doi.org/10.1073/pnas.0607177104>, PMID: 17360680
- Kotaleski JH, Lester D, Blackwell KT. 2002. Subcellular interactions between parallel fibre and climbing fibre signals in purkinje cells predict sensitivity of classical conditioning to interstimulus interval. *Integrative Physiological & Behavioral Science* **37**:265–292. DOI: <https://doi.org/10.1007/BF02734249>, PMID: 12645844
- Kristensen AS, Jenkins MA, Banke TG, Schousboe A, Makino Y, Johnson RC, Huganir R, Traynelis SF. 2011. Mechanism of Ca²⁺/calmodulin-dependent kinase II regulation of AMPA receptor gating. *Nature Neuroscience* **14**:727–735. DOI: <https://doi.org/10.1038/nn.2804>, PMID: 21516102
- Kubota S, Kitajima T. 2008. A model for synaptic development regulated by NMDA receptor subunit expression. *Journal of Computational Neuroscience* **24**:1–20. DOI: <https://doi.org/10.1007/s10827-007-0036-8>, PMID: 18202921
- Larkman AU, Jack JJ. 1995. Synaptic plasticity: hippocampal LTP. *Current Opinion in Neurobiology* **5**:324–334. DOI: [https://doi.org/10.1016/0959-4388\(95\)80045-X](https://doi.org/10.1016/0959-4388(95)80045-X), PMID: 7580155
- Lee KS. 1982. Sustained enhancement of evoked potentials following brief, high-frequency stimulation of the cerebral cortex in vitro. *Brain Research* **239**:617–623. DOI: [https://doi.org/10.1016/0006-8993\(82\)90538-8](https://doi.org/10.1016/0006-8993(82)90538-8), PMID: 6284309
- Lee H-K, Kirkwood A. 2011. AMPA receptor regulation during synaptic plasticity in Hippocampus and neocortex. *Seminars in Cell & Developmental Biology* **22**:514–520. DOI: <https://doi.org/10.1016/j.semcdb.2011.06.007>
- Li L, Lai M, Cole S, Le Novère N, Edelstein SJ. 2020. Neurogranin stimulates Ca²⁺/calmodulin-dependent kinase II by suppressing calcineurin activity at specific calcium spike frequencies. *PLOS Computational Biology* **16**:e1006991. DOI: <https://doi.org/10.1371/journal.pcbi.1006991>, PMID: 32049957
- Lisachev PD, Shtark MB. 2018. Long-term potentiation-associated gene expression: involvement of the tumour protein. In: Stuchlik A (Ed). *The Hippocampus-Plasticity and Functions*. IntechOpen. p. 1–53. DOI: <https://doi.org/10.5772/intechopen.73219>
- Lisman J. 1989. A mechanism for the Hebb and the anti-Hebb processes underlying learning and memory. *PNAS* **86**:9574–9578. DOI: <https://doi.org/10.1073/pnas.86.23.9574>, PMID: 2556718
- Ma L, Alonso A, Dickson CT. 2008. Differential induction of long-term potentiation in the horizontal versus columnar superficial connections to layer II cells of the entorhinal cortex. *Neural Plasticity* **2008**:1–12. DOI: <https://doi.org/10.1155/2008/814815>, PMID: 18604300
- Mäki-Marttunen T, Lines GT, Edwards AG, Tveito A, Dale AM, Einevoll GT, Andreassen OA. 2017. Pleiotropic effects of schizophrenia-associated genetic variants in neuron firing and cardiac pacemaking revealed by computational modeling. *Translational Psychiatry* **7**:5. DOI: <https://doi.org/10.1038/s41398-017-0007-4>, PMID: 30446648
- Mäki-Marttunen T, Hanes G, Devor A, Metzner C, Dale AM, Andreassen OA, Einevoll GT. 2018. A stepwise neuron model fitting procedure designed for recordings with high spatial resolution: application to layer 5 pyramidal cells. *Journal of Neuroscience Methods* **293**:264–283. DOI: <https://doi.org/10.1016/j.jneumeth.2017.10.007>, PMID: 28993204
- Mäki-Marttunen T, Krull F, Bettella F, Hagen E, Næss S, Ness TV, Moberget T, Elvsåshagen T, Metzner C, Devor A, Edwards AG, Fyhn M, Djurovic S, Dale AM, Andreassen OA, Einevoll GT. 2019. Alterations in Schizophrenia-

- Associated genes can lead to increased power in Delta oscillations. *Cerebral Cortex* **29**:875–891. DOI: <https://doi.org/10.1093/cercor/bhy291>, PMID: 30475994
- Manninen T**, Hituri K, Kotaleski JH, Blackwell KT, Linne ML. 2010. Postsynaptic signal transduction models for long-term potentiation and depression. *Frontiers in Computational Neuroscience* **4**:152. DOI: <https://doi.org/10.3389/fncom.2010.00152>, PMID: 21188161
- Markram H**, Muller E, Ramaswamy S, Reimann MW, Abdellah M, Sanchez CA, Ailamaki A, Alonso-Nanclares L, Antille N, Arsever S, Kahou GA, Berger TK, Bilgili A, Buncic N, Chalimourda A, Chindemi G, Courcol JD, Delalondre F, Delattre V, Druckmann S, et al. 2015. Reconstruction and simulation of neocortical microcircuitry. *Cell* **163**:456–492. DOI: <https://doi.org/10.1016/j.cell.2015.09.029>, PMID: 26451489
- Martin BS**, Huntsman MM. 2012. Pathological plasticity in fragile X syndrome. *Neural Plasticity* **2012**:1–12. DOI: <https://doi.org/10.1155/2012/275630>, PMID: 22811939
- Martinez EA**, Dietrich D. 2015. Buffer mobility and the regulation of neuronal calcium domains. *Frontiers in Cellular Neuroscience* **9**:48. DOI: <https://doi.org/10.3389/fncel.2015.00048>, PMID: 25750615
- McDougal RA**, Hines ML, Lytton WW. 2013. Reaction-diffusion in the NEURON simulator. *Frontiers in Neuroinformatics* **7**:28. DOI: <https://doi.org/10.3389/fninf.2013.00028>, PMID: 24298253
- Meunier CN**, Chameau P, Fossier PM. 2017. Modulation of synaptic plasticity in the cortex needs to understand all the players. *Frontiers in Synaptic Neuroscience* **9**:2. DOI: <https://doi.org/10.3389/fnsyn.2017.00002>, PMID: 28203201
- Michalski PJ**, Loew LM. 2012. CaMKII activation and dynamics are independent of the holoenzyme structure: an infinite subunit holoenzyme approximation. *Physical Biology* **9**:036010. DOI: <https://doi.org/10.1088/1478-3975/9/3/036010>, PMID: 22683827
- Mundorf ML**, Joseph JD, Austin CM, Caron MG, Wightman RM. 2001. Catecholamine release and uptake in the mouse prefrontal cortex. *Journal of Neurochemistry* **79**:130–142. DOI: <https://doi.org/10.1046/j.1471-4159.2001.00554.x>, PMID: 11595765
- Nevejan T**, Sakmann B. 2006. Spine Ca²⁺ signaling in spike-timing-dependent plasticity. *Journal of Neuroscience* **26**:11001–11013. DOI: <https://doi.org/10.1523/JNEUROSCI.1749-06.2006>, PMID: 17065442
- Neymotin SA**, McDougal RA, Bulanova AS, Zeki M, Lakatos P, Terman D, Hines ML, Lytton WW. 2016. Calcium regulation of HCN channels supports persistent activity in a multiscale model of neocortex. *Neuroscience* **316**:344–366. DOI: <https://doi.org/10.1016/j.neuroscience.2015.12.043>, PMID: 26746357
- Ninan I**, Arancio O. 2004. Presynaptic CaMKII is necessary for synaptic plasticity in cultured hippocampal neurons. *Neuron* **42**:129–141. DOI: [https://doi.org/10.1016/S0896-6273\(04\)00143-6](https://doi.org/10.1016/S0896-6273(04)00143-6), PMID: 15066270
- Oh MC**, Derkach VA, Guire ES, Soderling TR. 2006. Extrasynaptic membrane trafficking regulated by glur1 serine 845 phosphorylation primes ampa receptors for ltdp. *The Journal of Biological Chemistry* **281**:752–758. DOI: <https://doi.org/10.1074/jbc.M509677200>, PMID: 16272153
- Oh MC**, Derkach VA. 2005. Dominant role of the glur2 subunit in regulation of ampa receptors by camkii. *Nature Neuroscience* **8**:853. DOI: <https://doi.org/10.1038/nn1476>, PMID: 15924137
- Roche KW**, O'Brien RJ, Mammen AL, Bernhardt J, Huganir RL. 1996. Characterization of multiple phosphorylation sites on the AMPA receptor GluR1 subunit. *Neuron* **16**:1179–1188. DOI: [https://doi.org/10.1016/S0896-6273\(00\)80144-0](https://doi.org/10.1016/S0896-6273(00)80144-0), PMID: 8663994
- Roelfsema PR**, Holtmaat A. 2018. Control of synaptic plasticity in deep cortical networks. *Nature Reviews Neuroscience* **19**:166–180. DOI: <https://doi.org/10.1038/nrn.2018.6>, PMID: 29449713
- Sáez-Briones P**, Soto-Moyano R, Burgos H, Castillo A, Valladares L, Morgan C, Pérez H, Barra R, Constandil L, Laurido C, Hernández A. 2015. β 2-adrenoceptor stimulation restores frontal cortex plasticity and improves visuospatial performance in hidden-prenatally-malnourished young-adult rats. *Neurobiology of Learning and Memory* **119**:1–9. DOI: <https://doi.org/10.1016/j.nlm.2014.11.003>, PMID: 25464009
- Savtchenko LP**, Bard L, Jensen TP, Reynolds JP, Kraev I, Medvidov M, Stewart MG, Henneberger C, Rusakov DA. 2018. Astroglial biophysics probed with a realistic cell model. bioRxiv. *bioRxiv*. DOI: <https://doi.org/10.1101/336974>
- Seol GH**, Ziburkus J, Huang S, Song L, Kim IT, Takamiya K, Huganir RL, Lee HK, Kirkwood A. 2007. Neuromodulators control the polarity of spike-timing-dependent synaptic plasticity. *Neuron* **55**:919–929. DOI: <https://doi.org/10.1016/j.neuron.2007.08.013>, PMID: 17880895
- Shirai Y**, Kashiwagi K, Yagi K, Sakai N, Saito N. 1998. Distinct effects of fatty acids on translocation of gamma- and epsilon-subspecies of protein kinase C. *Journal of Cell Biology* **143**:511–521. DOI: <https://doi.org/10.1083/jcb.143.2.511>, PMID: 9786959
- Shouval H**, Intrator N, Cooper LN. 1997. BCM network develops orientation selectivity and ocular dominance in natural scene environment. *Vision Research* **37**:3339–3342. DOI: [https://doi.org/10.1016/S0042-6989\(97\)00087-4](https://doi.org/10.1016/S0042-6989(97)00087-4), PMID: 9425548
- Sjöström PJ**, Turrigiano GG, Nelson SB. 2001. Rate, timing, and cooperativity jointly determine cortical synaptic plasticity. *Neuron* **32**:1149–1164. DOI: [https://doi.org/10.1016/S0896-6273\(01\)00542-6](https://doi.org/10.1016/S0896-6273(01)00542-6), PMID: 11754844
- Sjöström PJ**, Rancz EA, Roth A, Häusser M. 2008. Dendritic excitability and synaptic plasticity. *Physiological Reviews* **88**:769–840. DOI: <https://doi.org/10.1152/physrev.00016.2007>, PMID: 18391179
- Song Q**, Zheng HW, Li XH, Huganir RL, Kuner T, Zhuo M, Chen T. 2017. Selective phosphorylation of AMPA receptor contributes to the network of Long-Term potentiation in the anterior cingulate cortex. *The Journal of Neuroscience* **37**:8534–8548. DOI: <https://doi.org/10.1523/JNEUROSCI.0925-17.2017>, PMID: 28765333
- Spruston N**, Jonas P, Sakmann B. 1995. Dendritic glutamate receptor channels in rat hippocampal CA3 and CA1 pyramidal neurons. *The Journal of Physiology* **482** (Pt 2):325–352. DOI: <https://doi.org/10.1113/jphysiol.1995.sp020521>, PMID: 7536248

- Sun X, Zhao Y, Wolf ME. 2005. Dopamine receptor stimulation modulates AMPA receptor synaptic insertion in prefrontal cortex neurons. *Journal of Neuroscience* **25**:7342–7351. DOI: <https://doi.org/10.1523/JNEUROSCI.4603-04.2005>, PMID: 16093384
- Toyoda H, Wu LJ, Zhao MG, Xu H, Jia Z, Zhuo M. 2007. Long-term depression requires postsynaptic AMPA GluR2 receptor in adult mouse cingulate cortex. *Journal of Cellular Physiology* **211**:336–343. DOI: <https://doi.org/10.1002/jcp.20940>, PMID: 17149707
- Tsumoto T. 1990. Long-term potentiation and depression in the cerebral neocortex. *The Japanese Journal of Physiology* **40**:573–593. DOI: <https://doi.org/10.2170/jjphysiol.40.573>, PMID: 1964984
- Urakubo H, Honda M, Froemke RC, Kuroda S. 2008. Requirement of an allosteric kinetics of NMDA receptors for spike timing-dependent plasticity. *Journal of Neuroscience* **28**:3310–3323. DOI: <https://doi.org/10.1523/JNEUROSCI.0303-08.2008>, PMID: 18367598
- Van den Oever MC, Goriounova NA, Li KW, Van der Schors RC, Binnekade R, Schoffelmeer AN, Mansvelter HD, Smit AB, Spijker S, De Vries TJ. 2008. Prefrontal cortex AMPA receptor plasticity is crucial for cue-induced relapse to heroin-seeking. *Nature Neuroscience* **11**:1053–1058. DOI: <https://doi.org/10.1038/nn.2165>, PMID: 19160503
- Wang JQ, Arora A, Yang L, Parelkar NK, Zhang G, Liu X, Choe ES, Mao L. 2005. Phosphorylation of AMPA receptors: mechanisms and synaptic plasticity. *Molecular Neurobiology* **32**:237–250. DOI: <https://doi.org/10.1385/MN:32:3:237>, PMID: 16385140
- Weber CR, Piacentino , Ginsburg KS, Houser SR, Bers DM. 2002. Na(+)-Ca(2+) exchange current and submembrane [Ca(2+)] during the cardiac action potential. *Circulation Research* **90**:182–189. DOI: <https://doi.org/10.1161/hh0202.103940>, PMID: 11834711
- Williamson T, Schwartz JM, Kell DB, Stateva L. 2009. Deterministic mathematical models of the cAMP pathway in *Saccharomyces cerevisiae*. *BMC Systems Biology* **3**:70. DOI: <https://doi.org/10.1186/1752-0509-3-70>, PMID: 19607691
- Xia J, Chung HJ, Wihler C, Haganir RL, Linden DJ. 2000. Cerebellar long-term depression requires PKC-regulated interactions between GluR2/3 and PDZ domain-containing proteins. *Neuron* **28**:499–510. DOI: [https://doi.org/10.1016/S0896-6273\(00\)00128-8](https://doi.org/10.1016/S0896-6273(00)00128-8), PMID: 11144359
- Xu TX, Ma Q, Spealman RD, Yao WD. 2010. Amphetamine modulation of long-term potentiation in the prefrontal cortex: dose dependency, monoaminergic contributions, and paradoxical rescue in hyperdopaminergic mutant. *Journal of Neurochemistry* **115**:1643–1654. DOI: <https://doi.org/10.1111/j.1471-4159.2010.07073.x>, PMID: 20969573
- Xue B, Edwards MC, Mao LM, Guo ML, Jin DZ, Fibuch EE, Wang JQ. 2014. Rapid and sustained GluA1 S845 phosphorylation in synaptic and extrasynaptic locations in the rat forebrain following amphetamine administration. *Neurochemistry International* **64**:48–54. DOI: <https://doi.org/10.1016/j.neuint.2013.11.001>, PMID: 24231469
- Zhao Y, Chen S, Swensen AC, Qian WJ, Gouaux E. 2019. Architecture and subunit arrangement of native AMPA receptors elucidated by cryo-EM. *Science* **364**:355–362. DOI: <https://doi.org/10.1126/science.aaw8250>, PMID: 30975770
- Zhou HC, Sun YY, Cai W, He XT, Yi F, Li BM, Zhang XH. 2013. Activation of β 2-adrenoceptor enhances synaptic potentiation and behavioral memory via cAMP-PKA signaling in the medial prefrontal cortex of rats. *Learning & Memory* **20**:274–284. DOI: <https://doi.org/10.1101/lm.030411.113>, PMID: 23596314